



Earth Sciences

Fracturation pattern and morphostructure of the Deception Island volcano, South Shetland Islands, Antarctica

Adolfo Maestro¹ , Fernando Bohoyo¹, Thomas Schmid² and Jerónimo López-Martínez³

¹Instituto Geológico y Minero de España, IGME-CSIC, Tres Cantos, Madrid, Spain; ²Centro de Investigaciones Energéticas, Medioambientales y Tecnológicas, CIEMAT, Madrid, Spain and ³Universidad Autónoma de Madrid, Facultad de Ciencias, Campus de Cantoblanco, Madrid, Spain

Abstract

The Antarctic active volcano Deception Island has been the subject of extensive geological, geophysical and geomorphological research, including studies on its volcanic history. Since the initial geoscientific research, many authors have included lineament traces (in general considered as faults) in the maps, schemes and figures accompanying their publications. In the last 3 decades, several papers have contributed to improving our understanding of the volcano's structure. In some cases, the fracture network was identified, measured and analysed and general models of the island's structure were developed. However, the various authors have not always used consistent methodologies for lineament mapping, presenting significant disparities in the obtained results. This paper analyses previously interpreted lineaments and integrates existing geophysical, geological and morphostructural evidence, along with original field data, to establish a morphostructural model through a coherence and uncertainty analysis. The lineaments determined on Deception Island exhibit three preferred directions: NE-SW, ESE-WSW and SSE-NNW. However, the fractures measured in the field generally show a radial distribution, although there are two preferred directions: NNE-SSW and SE-NW. A synthetic map of Deception Island's lineaments is presented, indicating which are the lineaments that should be considered tectonic-volcanic fractures among the other existing lineaments.

Keywords: Bransfield Basin; faults; lineaments; northern Antarctic Peninsula region; tectonics; volcanism

Introduction and geological setting

Deception Island is one of the most active volcanoes in Antarctica and, jointly with Mount Erebus, one of the two volcanoes to have produced the most recent eruptions (Smellie *et al.* 2021). After several eruptions in historical times, the most recent ones occurred in 1967, 1969 and 1970, damaging two of the existing scientific stations as well as producing geomorphological changes in several sectors of the island (Smellie & López-Martínez 2002). This Quaternary active volcano is situated in the south-western part of the Bransfield Basin, which is a young marginal basin (< 1.4 Ma) between the Antarctic Peninsula and the South Shetland Islands (Fig. 1a,b; Lawver *et al.* 1995). Deception Island is part of a volcanic ridge associated with the extensional structure of the Bransfield Basin, being a consequence of back-arc extension linked to the subduction of the Phoenix Plate beneath the Antarctic Plate (Barker 1982, González-Ferrán 1985, Barker & Austin 1994, Galindo-Zaldivar *et al.* 1996, McCarron & Larter 1998, González-Casado *et al.* 2000). Along with Deception Island (Fig. 1c), nearby volcanic islands such as Penguin and Bridgeman islands also exhibit Quaternary magmatism related to rifting (Birkenmajer *et al.* 1990, Gràcia *et al.* 1996, 1997, Haase *et al.* 2012).

Corresponding author: Adolfo Maestro; Email: a.maestro@igme.es

Cite this article: Maestro, A., Bohoyo, F., Schmid, T., & López-Martínez, J. 2025. Fracturation pattern and morphostructure of the Deception Island volcano, South Shetland Islands, Antarctica. *Antarctic Science*, 176–200. <https://doi.org/10.1017/S0954102025000124>

Deception Island is the onshore expression of a volcanic edifice with a basal diameter of ~30 km and a maximum height of 539 m above sea level in Mount Pond. It forms a horseshoe-shaped island around a 7 × 10 km caldera flooded by the sea, known as Port Foster (Fig. 1; Smellie 1988, Smellie & López-Martínez 2002, Barclay *et al.* 2009). Deception Island has thick ice cover that is mainly located in the eastern and south-western sectors, restricting the extent of rocky outcrops where observations can be made. Magnetic polarity and K-Ar data indicate that the exposed rocks are younger than 0.75 Ma and that the subaerial portion of the island was constructed primarily over the last 0.2 Ma (Valencio *et al.* 1979, Keller *et al.* 1992).

The volcanic evolution of Deception Island is divided into three key phases: pre-, syn- and post-caldera (Smellie 2001). The pre-caldera phase saw the formation of a subaerial volcanic shield and multiple coalesced shoaling seamounts, represented by the Basaltic Shield Formation. The syn-caldera phase was marked by the caldera's collapse, depositing pyroclastic deposits from the Outer Coast Tuff Formation, which forms an almost continuous outcrop along the island's outer part. These formations constitute the so-called Port Foster Group (Smellie 2001, 2002). The caldera collapse event has been dated to be between 8300 (Oliva-Urcía *et al.* 2015) and 3980 (Antoniades *et al.* 2018) BCE. Post-caldera volcanism includes over 70 eruptive vents scattered across the island, with more than 30 eruptions occurring during the Holocene, including over 20 in the past 2 centuries (Orheim 1972, López-Martínez *et al.* 2002). These vents, primarily associated with phreatomagmatic eruptions, deposited pyroclastic sediments over

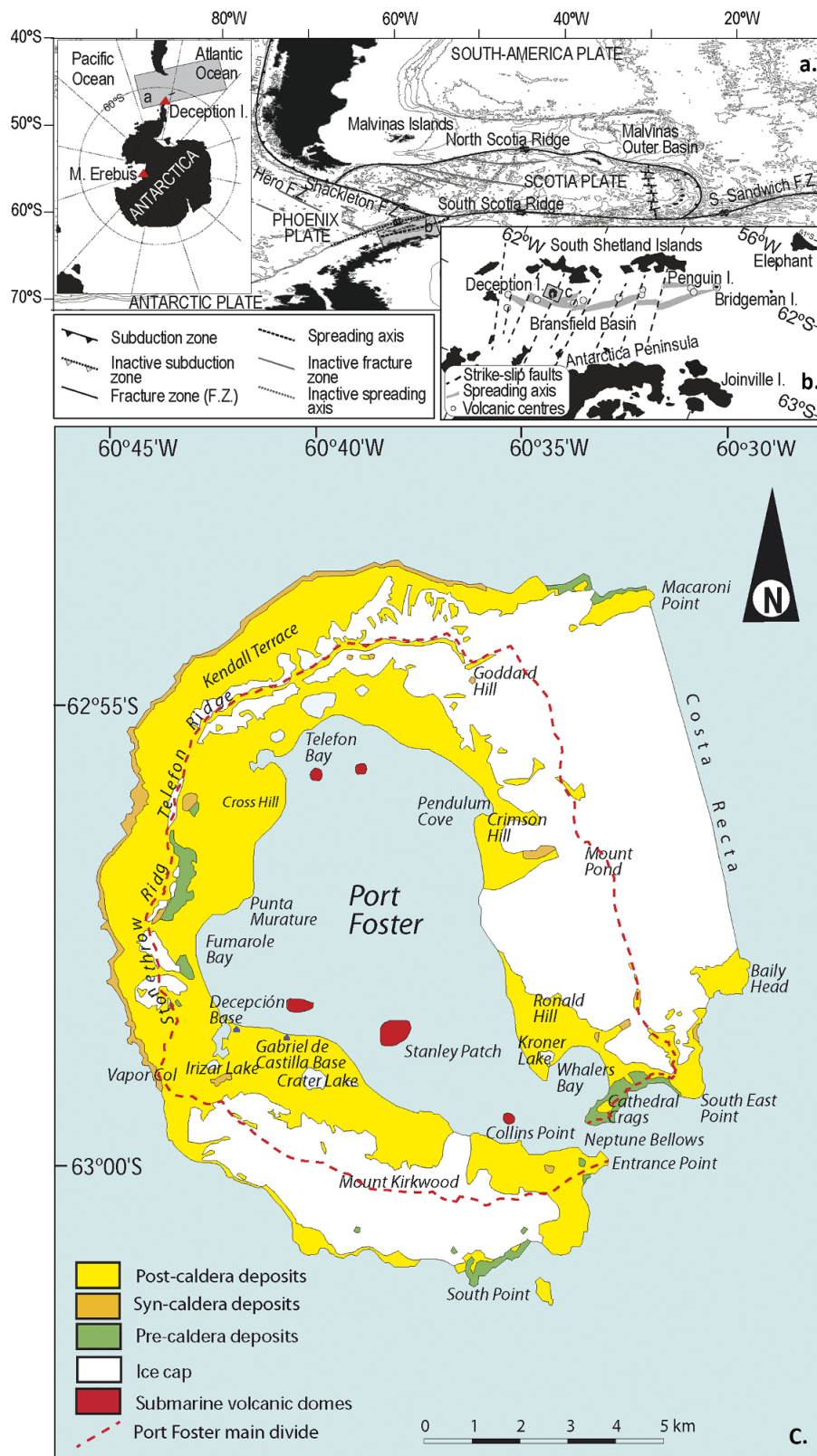


Figure 1. a. Regional tectonic framework of the Scotia Arc and north-western Antarctic Peninsula region. The Bransfield Trough area is marked by the box. b. Tectonic and geographical location of Deception Island along the spreading axis of the Bransfield Trough (modified from Grad *et al.* 1992, Barker & Austin 1994, Rey *et al.* 1997). c. Simplified geological sketch map of Deception Island (modified from Smellie & López-Martínez 2000, Smellie 2001).

pre- and syn-caldera deposits (Fig. 1d; Smellie 2001, 2002, Pedrazzi *et al.* 2018). These post-caldera units have been named by Smellie (2001, 2002) as the Mount Pond Group.

The caldera formation seems to be conditioned by a combination of regional tectonic and volcano-induced stresses (Smellie & López-Martínez 2002). The combination of these processes has led to the development of a series of discontinuities that, associated with volcanic activity, have generated fractures and various morphostructural features. A good number of lineaments have been represented in the maps, schemes and figures of some of the many existing publications on the geology, geophysics and geomorphology of Deception Island. However, it seems that not all of these various authors have used similar criteria to identify the lineaments, resulting in a complex and confusing network when all of the lineaments identified in the various publications are represented together (Fig. 2).

The aim of this paper is to analyse the proposals of these various authors, as well as our own data, in order to obtain a synthetic image of the tectonic-volcanic lineaments of Deception Island. The proposed map also considers other existing geophysical, geological and morphostructural evidence and identifies which of the existing lineaments should be considered unequivocally connected to the tectonic and volcanic evolution of Deception Island, including the caldera formation.

Data and methodology of the structural analysis

The basic information for this study comes from previous works published by various authors from 1961 to the present, among which the most recent study analysing the fracturing directions of Deception Island was carried out in 2021. These studies have focused on the qualitative and quantitative description of the morphostructural elements observed on Deception Island. The characterized morphostructural elements are located both in the emerged area of Deception Island and in the submerged part of its inner bay (Port Foster), and they mainly consist of lineaments, fractures (faults, joints and dykes), volcanic buildings and areas of fumarolic activity and thermal anomalies. Information related to this topic has been compiled from 40 articles. The lineament and fracturing data were analysed using statistical software (*Grapher* v.7.01870 by Golden Software, Inc., 2007; and *Stereonet* v.8 by R. Allmendinger, 2013) to establish frequency orientation diagrams in the form of rose diagrams and smoothed frequency curves. The smoothed frequency curves were prepared using the technique proposed by Wise & McCrory (1982) to eliminate the intrinsic dispersion of lineament orientations due to the methodology used in their determination, utilizing the concept of moving average windows to better determine the mode of each dataset. In the case of lineaments, the rose diagrams have been weighted according to their length, so that longer lineaments have greater representativeness.

Identified lineaments

The study of the lineaments identified on Deception Island consisted of the compilation and extraction of the traces of possible fractures or other morphotectonic discontinuities existing in previous cartographies. The review revealed that the information used for the creation of the maps comes from three sources: 1) geological observations and measurements on data collected from the island's surface during reconnaissance itineraries (Hawkes 1961, González-Ferrán & Katsui 1970, Dalziel *et al.* 1989, Martí *et al.* 1990, 1996, 2013, Birkenmajer 1992, 1995, Baraldo 1999, Baraldo

& Rinaldi 2000, López-Martínez *et al.* 2000, Smellie & López-Martínez 2000, Pérez-López *et al.* 2007, 2008), 2) the analysis of satellite images, digital terrain models and aerial photographs that provided a synoptic view of the terrain and enabled the identification of physiographical lineaments (Martí *et al.* 1996, Baraldo 1999, Baraldo & Rinaldi 2000, López-Martínez *et al.* 2000, Smellie & López-Martínez 2000, Paredes *et al.* 2006, 2007, Pérez-López *et al.*, 2007, 2008, Dunaev *et al.* 2021) and 3) geophysical interpretations and recordings using magnetic, gravimetric and seismic techniques, as well as geochemical prospecting campaigns on land and at sea (Martí *et al.* 1990, 1996, Rey *et al.* 1990, 1992, 1995, 1997, 2002, Carbó *et al.* 2001, Navarro *et al.* 2002, Somoza *et al.* 2004, Muñoz-Martin *et al.* 2005, Catalán *et al.* 2014, Pueyo *et al.* 2014, Belyaev *et al.* 2024). In some cases, the lineaments mapped in the analysed articles come from the combination of several of the sources described (Rey *et al.* 1990, 1995, 1997, 2002, Vila *et al.* 1992, González-Casado *et al.* 1999, Somoza *et al.* 2004, Paredes *et al.* 2006, 2007, Bonatto *et al.* 2007, Maestro *et al.* 2007, Berrocoso *et al.* 2012, Pedrera *et al.* 2012, Martí *et al.* 2013, Torrecillas *et al.* 2013, Bartolini *et al.* 2014, Lopes *et al.* 2015, Muniz *et al.* 2018, Álvarez-Valero *et al.* 2020, Hopfenblatt *et al.* 2021, Jiménez-Morales 2021). Before discussing the results obtained from the analysis of this information, it is important to highlight the characteristics and limitations of each procedure used by the various authors to determine the lineaments.

On the one hand, the fractures identified in outcrops in the field often have a lateral continuity that is difficult to determine due to reasons such as them being covered by later deposits, fault planes curving as they cross geological units with different rheological behaviours (Woodcock & Fischer 1986) or faults arranged *en echelon* (or staggered), relayed or anastomosed depending on how the slip is distributed based on the rheological conditions and the total stress that needs to be accommodated (Davis & Reynolds 1996). These factors lead to a high degree of subjectivity in extending tectonic structures beyond where they are clearly observed, which must be considered in any analysis.

On the other hand, although lineaments observed in satellite images, digital terrain models and aerial photographs sometimes correspond to identifiable faults, fractures or dykes in the field, there are many situations in which these features cannot be located in the studied areas due to the level of detail in the observations. The tectonic significance of the lineaments has been much debated, and two trends can be distinguished from discussions of this: 1) lineaments are linear discontinuities directly related to faults and fractures, excluding other phenomena (Cazabat 1975), and 2) lineaments are linear discontinuities with a composite nature, associated with landscape morphological elements and various tectonic phenomena (Chukwu-Ike & Norman 1977, Scanvic 1989). This second definition is likely to be more accurate, as there is usually a clear relationship between the linear feature and the terrain morphology. However, identifying lineaments with discontinuities or geological structures occurs only occasionally (Cortés *et al.* 1998, 2003). Some lineaments, especially large ones, represent surface manifestations of diverse structural elements along their paths, grouping together fractures, topographical depressions and boundaries of lithological or structural domains (Scanvic 1989).

Finally, the results of data analysis from geophysical methods enable the identification of gradient changes in gravimetric and magnetic anomalies, which help define lineaments, lithological contacts and potential faults at the crustal level, delimiting first-order structures. In addition, the interpretation of high-resolution seismic profiles helps to establish the most relevant tectonic

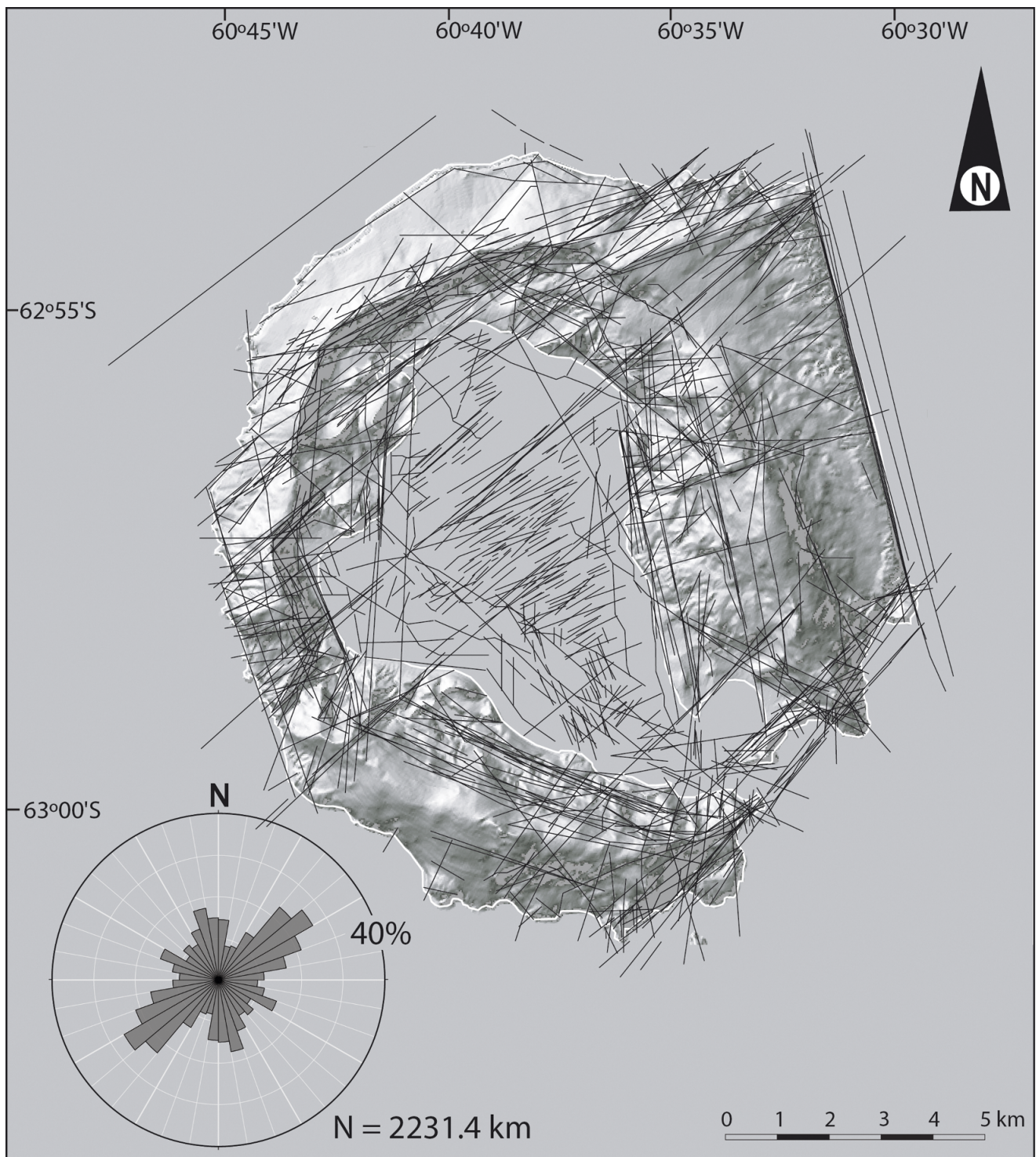


Figure 2. Joint representation in a single map of all of the lineaments proposed by the various authors mentioned in the text and analysed in this study, obtained from aerial photography, satellite images, digital terrain models and field data. The rose diagram shows the length-weighted orientations of all of the lineaments. The outer circle represents 40% of the data and N indicates the total length of all lineaments.

structures affecting the more recent units, and when a significant grid of seismic profiles is available, the length, direction and offset of faults can be reliably determined.

The lineaments defined by various authors have been vectorized from the published images. The resulting vector file is analysed using an automatic exploration program (*DXFLINES* developed by R. Merinero, unpublished). The exploration program used reads

vectorial format files, scanning first along the x -axis and then along the y -axis, following the sequence in which the lines were drawn. The program generates a file including for each line the (x, y) coordinates of its ends, its length in metres and its angle in degrees reckoned clockwise positive from north. The projection and coordinate system used in our analysis is UTM Zone 20S and WGS84 datum.

Fracture study

There are few studies in which systematic measurements of fractures affecting the volcanic units on Deception Island have been conducted (Maestro *et al.* 2007, Paredes *et al.* 2007, Pérez-López *et al.* 2007, 2008). The brittle structures measured can be classified into three categories according to the relative displacement between the blocks on either side: 1) joints, where no relative movement between the blocks occurs, for which the direction, dip and dip direction of the joint planes were considered, 2) dykes, related to the intrusion of basic rocks along fracture planes, for which the direction, dip and dip direction of the fracture planes through which the igneous material ascended were measured, and 3) faults, where the blocks slide relative to each other. Due to the lithological characteristics of the volcanic rocks outcropping on Deception Island, faults were characterized solely according to four parameters: fault plane direction, dip, dip direction and sense of movement, as slickensides are difficult to observe on the fault planes.

Correlation between lineaments and fractures measured in the field

Visually, a comparison can be made between the different frequency curves that show the orientations of the lineaments determined by various authors, as well as the fracture data (faults, joints and dykes) measured in different outcrops located within the different volcanic units that constitute Deception Island. To minimize the subjective effect of visual comparison, a correlation analysis was also performed to determine the relationship between the different frequency curves of the lineament orientations. For this, Spearman's correlation (r_s) was used, as it is one of the most commonly used methods to assess the relationship between two variables whose data do not follow a normal distribution (Sheskin 2000, Chok 2010). Furthermore, Spearman's correlation enables the use of data ranks instead of the raw data, meaning that the correlation between the different smoothed frequency curves obtained from the weighted data of the lineament directions could be calculated.

Spearman's correlation is defined by Equation 1:

$$r_s = 1 - \frac{6 \cdot \sum d_i^2}{n \cdot (n^2 - 1)} \quad (1)$$

where d is the difference in the frequency ranks between the two variables being compared, which have the same direction, and n is the number of data pairs (in this case, directions), which in our case come to 180 (from 0° to 180° , $0^\circ = 180^\circ$). Spearman's correlation coefficient varies between -1 and 1, and it allows us to determine the direction and strength of the correlation. If we have a correlation coefficient between -1 and < 0 , there is a negative correlation between the analysed variables; if the correlation coefficient varies between > 0 and 1, the correlation is positive; and if the coefficient is 0, there is no correlation. In our analysis, only positive correlations were considered. To determine the strength of the correlation, we applied the distribution proposed by Kuckartz *et al.* (2013), who established the following intervals for r_s values: between 0.0 and < 0.1 , there is no correlation; between 0.1 and < 0.3 , there is a weak correlation; between 0.3 and < 0.5 , the correlation is moderate; between 0.5 and < 0.7 , the correlation is strong; and between 0.7 and 1.0, the correlation is very strong. In this study, only correlations that varied between moderate and very strong were considered (Table 1).

Distribution of heated ground, fumaroles, volcanic structures and earthquake epicentres

Volcanic structures, fumaroles and heated ground have been mapped based on existing information from various works (López-Martínez *et al.* 1996, 2000, Smellie & López-Martínez 2000, Somoza *et al.* 2004, Caselli *et al.* 2007, Martí *et al.* 2013, Pedrazzi *et al.* 2020, Hopfenblatt *et al.* 2021). In addition to the main volcanic structure and the caldera, there are many smaller volcanic features, such as tuff cones, tuff rings and ash cones. Most cones and craters are located inside the caldera, where their original shapes can be reconstructed and mapped. The areas with the highest concentration of craters are around Telefon Bay and along the northern slope of Mount Kirkwood ridge. In the Telefon Bay area, craters that originated during the 1967 and 1970 eruptions are well preserved, with some of them being occupied by lakes. Some noticeable depressions and scarps, of varying sizes, discernible in several places within the glaciers, have been interpreted as subglacial structural features. The most notable are those approximately parallel to the main divide of the island, located on both sides of Mount Pond (López-Martínez *et al.* 2000), particularly to the east of Goddard Hill and on the western side of Mount Pond. These depressions, with diameters ranging from 100 to 300 m, have margins that are locally indistinct, and the ice cracks in their vicinity are subparallel to their edges. López-Martínez & Serrano (2002) interpreted these depressions as the result of recent or even ongoing thermal activity beneath the ice.

Thermal anomalies can be observed in various locations on the island, where fumaroles, hot soils or deposits from fumarolic activity are present. Most evidence of thermal activity is found along the coast of Port Foster. However, fumaroles are also present to the north of Mount Pond, north of Whalers Bay, north-west of Deception Base (Argentina) and on the western slopes of Stonethrow Ridge, west of Fumarole Bay. The highest temperatures recorded ($\sim 108^\circ\text{C}$) were measured in Fumarole Bay (López-Martínez *et al.* 1996, 2000, Villegas *et al.* 1997, Smellie & López-Martínez 2000, Caselli *et al.* 2004, Kusakabe *et al.* 2009).

Although seismic monitoring of the Deception Island volcano began in the 1950s, it was abandoned after the 1967–1970 eruptions. It was not until 1994 that the Andalusian Institute of Geophysics (University of Granada, Spain) began to systematically study the seismic activity (e.g. Almendros *et al.* 1997, 1999, 2018, 2020), which was continued by the Spanish National Geographical Institute (IGN) from 2022. Initially, seismic monitoring was limited to summer periods (December–February), until a permanent station was deployed in 2008 (e.g. Carmona *et al.* 2014). Over the last 3 decades, Deception Island's volcanic seismicity has shown a continuous background of long-period events and tremors, related to the activity of the shallow hydrothermal system (Carmona *et al.* 2012). This situation defines the latent state of the volcano. However, seismic activity has intensified on at least three recent occasions: in 1992 (Ortiz *et al.* 1997), in 1999 (Ibáñez *et al.* 2003) and in 2015 (Almendros *et al.* 2018). These activities were characterized by an increase in the number and energy of seismic events and the appearance of a large number of volcano-tectonic earthquakes caused by fractures within the volcanic edifice. Epicentre data from the years 1999 and 2015 were published by Moreno-Vacas & Almendros (2021), and data from 1999 and 2009–2020 were provided by the Andalusian Institute of Geophysics (University of Granada; Carmona *et al.* 2012, Almendros *et al.* 2018), with additional data provided by the IGN from 2022 to 2024.

Table 1. Spearman's correlation coefficient values for the different variables analysed in this study: 1) fractures measured in the rocky outcrops of Deception Island (normal, reverse, dextral and sinistral faults, diclases and dykes) and 2) lineaments proposed by the various authors analysed in this study based on the interpretation of aerial photographs, satellite images, digital terrain models and field data. If the correlation coefficient varies between -1 and < 0 then the correlation between the variables is negative; if the correlation coefficient varies between > 0 and 1 then the correlation between the variables is positive; and if the coefficient is 0 then there is no correlation. For correlation coefficient values between 0.0 and < 0.1, there is no correlation; for correlation coefficient values between 0.1 and < 0.3, there is weak correlation; for correlation coefficient values between 0.3 and < 0.5, the correlation is moderate; for correlation coefficient values between 0.5 and < 0.7, the correlation is strong; and for correlation coefficient values between 0.7 and 1.0, the correlation is very strong. In this study, only moderate (orange), strong (yellow) and very strong (green) positive correlation ratios have been considered.

Variable	Fractures	Faults	Joints	Dykes	Normal faults	Reverse faults	Strike-slip faults	Dextral faults	Sinistral faults	Hawkes (1961)	González Ferrán & Katsui (1970)	Dalziel <i>et al.</i> (1979)	Martí <i>et al.</i> (1990)	Birkenmajer (1992)	Martí <i>et al.</i> (1996)	Baraldo (1999)	López-Martínez (2002)	Paredes <i>et al.</i> (2006)	Paredes <i>et al.</i> (2007)	Martí <i>et al.</i> (2013)	Dunaev <i>et al.</i> (2021)
Fractures	1	0.926	0.639	0.146	0.725	0.473	0.608	0.370	0.474	0.131	-0.624	0.451	0.041	-0.226	-0.054	-0.217	-0.163	-0.581	-0.006	-0.109	-0.192
Faults	0.926	1	0.370	-0.089	0.910	0.232	0.599	0.509	0.377	0.177	-0.633	0.280	-0.035	-0.022	-0.099	-0.227	-0.279	-0.599	0.055	-0.083	-0.176
Joints	0.639	0.370	1	0.397	0.062	0.668	0.314	0.096	0.328	0.019	-0.376	0.444	0.014	-0.314	-0.203	-0.249	-0.136	-0.482	-0.231	-0.239	-0.294
Dykes	0.146	-0.089	0.397	1	-0.346	0.407	0.445	-0.182	0.739	0.057	0.246	0.321	0.573	-0.261	0.622	0.205	-0.097	0.203	-0.007	0.157	0.341
Normal faults	0.725	0.910	0.062	-0.346	1	-0.090	0.456	0.563	0.171	0.177	-0.601	0.013	-0.147	0.225	-0.150	-0.264	-0.312	-0.579	0.021	-0.134	-0.205
Reverse faults	0.473	0.232	0.668	0.407	-0.090	1	0.189	-0.176	0.382	0.297	-0.121	0.838	0.234	-0.770	-0.020	0.185	0.245	-0.085	0.170	0.234	-0.039
Strike-slip faults	0.608	0.599	0.314	0.445	0.456	0.189	1	0.654	0.787	0.424	0.097	0.265	0.443	-0.060	0.506	-0.084	-0.409	-0.238	0.174	0.214	0.037
Dextral faults	0.370	0.509	0.096	-0.182	0.563	-0.176	0.654	1	0.097	0.441	-0.060	-0.108	-0.207	0.241	-0.060	-0.557	-0.659	-0.312	-0.160	-0.194	-0.528
Sinistral faults	0.474	0.377	0.328	0.739	0.171	0.382	0.787	0.097	1	0.284	0.167	0.420	0.746	-0.231	0.678	0.368	-0.102	-0.081	0.342	0.443	0.496
Hawkes (1961)	0.131	0.177	0.019	0.057	0.177	0.297	0.424	0.441	0.284	1	0.288	0.404	0.185	-0.195	0.066	0.179	-0.224	-0.104	0.369	0.399	-0.069
González-Ferrán & Katsui (1970)	-0.624	-0.633	-0.376	0.246	-0.601	-0.121	0.097	-0.060	0.167	0.288	1	-0.022	0.469	-0.119	0.484	0.387	0.169	0.508	0.393	0.553	0.338
Dalziel <i>et al.</i> (1989)	0.451	0.280	0.444	0.321	0.013	0.838	0.265	-0.108	0.420	0.404	-0.022	1	0.289	-0.772	0.141	0.412	0.318	0.018	0.527	0.529	0.185
Martí <i>et al.</i> (1990)	0.041	-0.035	0.014	0.573	-0.147	0.234	0.443	-0.207	0.746	0.185	0.469	0.289	1	-0.131	0.784	0.685	0.154	-0.004	0.526	0.699	0.712
Birkenmajer (1992)	-0.226	-0.022	-0.314	-0.261	0.225	-0.770	-0.060	0.241	-0.231	-0.195	-0.119	-0.772	-0.131	1	-0.111	-0.262	-0.609	-0.350	-0.261	-0.341	-0.030
Martí <i>et al.</i> (1996)	-0.054	-0.099	-0.203	0.622	-0.150	-0.020	0.506	-0.060	0.678	0.066	0.484	0.141	0.784	-0.111	1	0.464	0.127	0.374	0.333	0.537	0.618
Baraldo (1999)	-0.217	-0.227	-0.249	0.205	-0.264	0.185	-0.084	-0.557	0.368	0.179	0.387	0.412	0.685	-0.262	0.464	1	0.502	0.187	0.797	0.868	0.891
López-Martínez <i>et al.</i> (2002)	-0.163	-0.279	-0.136	-0.097	-0.312	0.245	-0.409	-0.659	-0.102	-0.224	0.169	0.318	0.154	-0.609	0.127	0.502	1	0.376	0.349	0.374	0.357
Paredes <i>et al.</i> (2006)	-0.581	-0.599	-0.482	0.203	-0.579	-0.085	-0.238	-0.312	-0.081	-0.104	0.508	0.018	-0.004	-0.350	0.374	0.187	0.376	1	0.064	0.197	0.216
Paredes <i>et al.</i> (2007)	-0.006	0.055	-0.231	-0.007	0.021	0.170	0.174	-0.160	0.342	0.369	0.393	0.527	0.526	-0.261	0.333	0.797	0.349	0.064	1	0.909	0.675
Martí <i>et al.</i> (2013)	-0.109	-0.083	-0.239	0.157	-0.134	0.234	0.214	-0.194	0.443	0.399	0.553	0.529	0.699	-0.341	0.537	0.868	0.374	0.197	0.909	1	0.735
Dunaev <i>et al.</i> (2021)	-0.192	-0.176	-0.294	0.341	-0.205	-0.039	0.037	-0.528	0.496	-0.069	0.338	0.185	0.712	-0.030	0.618	0.891	0.357	0.216	0.675	0.735	1

All of these elements, including also volcanic structures, fumaroles, heated ground and earthquake epicentres, were digitized in a Geographical Information System program. This information was then used to create a density map to observe the general pattern and to highlight preferred directions. Density maps were estimated using a two-dimensional, symmetric Gaussian kernel density method (e.g. Kiyosugi *et al.* 2012, Mazzarini *et al.* 2016). Kernel density estimation is a non-parametric way to estimate the probability density function of features within a region around those features. The density map was generated using *ArcGIS Pro* software and was determined according to Equation 2:

$$Density = \frac{1}{(radius)^2} \sum_{i=1}^n \left[\frac{3}{\pi} * pop_i \left(1 - \left(\frac{dist_i}{radius} \right)^2 \right)^2 \right] \quad (2)$$

where $i = 1, \dots, n$ are the input points within the radius of the location (x, y) , pop_i is the population field value of point i , and $dist_i$ is the distance between point i and the location (x, y) . The cell size for the output raster dataset is the shorter of the width or height of the output extent in the output spatial reference, divided by 250. Finally, a specific variable bandwidth value was calculated for the input dataset using a spatial variant of Silverman's rule of thumb (Silverman 1986), which is robust for outlier points. *ArcGIS* applies Equation 3 to calculate the bandwidth:

$$Bandwidth = 0.9 * \min \left(SD, \sqrt{\frac{1}{\ln(2)}} * D_m \right) * n^{-0.2} \quad (3)$$

where D_m is the (weighted) median distance from the (weighted) mean centre, n is the number of points and SD is the standard distance.

Results

The analysis includes the distribution of volcanic edifices, locations with evidence of thermal and geochemical anomalies related to heated ground and fumaroles, earthquake epicentres, linear elements identified in aerial photographs, satellite images and in the digital terrain model and fractures measured in rock outcrops. This has allowed us to characterize the preferred orientations in which these features are distributed, both on the emerged surface of Deception Island and in its submerged part in Port Foster and the surrounding areas in the Bransfield Strait.

Lineaments identified on Deception Island

A total of 40 scientific publications have been analysed that, although in many cases not as their primary goal, include maps or schemes of lineaments or determine the existence of linear structures controlling the physiography and structure of Deception Island. For a detailed analysis, these works have been grouped into three categories based on the methodology used to determine the lineaments: 1) mapping of lineaments based on geological observations and fracturing data taken from rock outcrops on the island, as well as interpretations from satellite images, digital terrain models and aerial photographs conducted by the authors without relying on prior data (Hawkes 1961, González-Ferrán & Katsui 1970, Dalziel *et al.* 1989, Martí *et al.* 1990, 1996, 2013, Birkenmajer 1992, Baraldo 1999, López-Martínez *et al.* 2000, Smellie & López-Martínez 2000, Paredes *et al.* 2006, 2007, Dunaev *et al.* 2021), 2) cartographies of linear structures based on the

interpretation of geophysical data (Rey *et al.* 1990, 1992, 2002, Carbó *et al.* 2001, Navarro *et al.* 2002, Muñoz-Martín *et al.* 2005, Catalán *et al.* 2014, Pueyo *et al.* 2014) and 3) distributions of chemical elements in sediments or on the sea surface in Port Foster (Rey *et al.* 1997, Somoza *et al.* 2004, Belyaev *et al.* 2024). The rest of the studies analysed compile information from previous publications, so the data that they provide would be repetitive and have not been used in this study.

Considering their direction and length, the lineaments determined on Deception Island and mapped in the various scientific papers analysed in this study exhibit three preferred directions: N050E, N110E and N170E (Fig. 2). The cartographies by Hawkes (1961), González-Ferrán & Katsui (1970) and Birkenmajer (1992) focus on morphostructural features related to the collapse of the volcanic edifice, emphasizing concentric and radial structures to the caldera (Fig. 3). Hawkes (1961) presents an absolute maximum in orientation N115E and three relative maxima in orientations N025E, N050E and N165E; González-Ferrán & Katsui (1970) show an absolute maximum of direction N165E and three relative maxima of direction N005E, N055E and N095E; and Birkenmajer (1992) displays two absolute maxima of direction N165E and N005E and two relative maxima of direction N035E and N085E.

Dalziel *et al.* (1989) identified a set of lineaments showing a main direction, N045E, and a secondary one, N115E (Fig. 3). Martí *et al.* (1990), based on field data, photointerpretation and seismic profiles obtained in Port Foster interpreted by Rey *et al.* (1990), determine the existence of a main lineament direction, N050E, and three secondary directions, N005E, N105E and N155E (Fig. 3). Later, these same authors modify their interpretations: Martí *et al.* (1996) establish a main direction, N065E, and three secondary orientations, N045E, N115E and N175E (Fig. 3); and Martí *et al.* (2013) present two main sub-perpendicular lineament directions, N055E and N165E, and a secondary orientation, N115E (Fig. 3). Baraldo (1999), in his morphostructural interpretation, which also simplifies the information on fault orientations obtained by Rey *et al.* (1992) in Port Foster from seismic profiles, establishes two main lineament directions, N045E and N165E (Fig. 3). López-Martínez *et al.* (2000) and Smellie & López-Martínez (2000), in their geomorphological and geological maps at 1:25 000 scale of the island, respectively, represent the same main faults affecting the different emerged volcanic units of Deception Island, and, the first of the two mentioned maps also incorporates information from Port Foster, based on Rey *et al.*'s (1992) seismic profile interpretation, establishing a main lineament orientation, N055E, and a secondary sub-perpendicular direction, N140E (Fig. 3). Paredes *et al.* (2006) conducted a detailed mapping of linear elements identified through morphometric analysis of the digital elevation model of both the emerged zone and Port Foster, obtaining two main directions, N085E and N175E, and two secondary directions, N065E and N115E (Fig. 3). Paredes *et al.* (2007) reinterpreted the information from their previous work, and, by synthesizing bibliographic work from various authors, conducting morphometric analysis of the relief and processing aerial images, they established the existence of a main lineament direction, N055E, and three secondary orientations, N115E, N135E, and N165E (Fig. 3). Finally, Dunaev *et al.* (2021) conducted a structural-geomorphological interpretation using satellite imagery, bathymetric and topographic data and bibliographic data on the geological-geomorphological structure and geophysical investigations of the island. They established a number of lineaments with two main directions, N045E and N165E, and two secondary directions, N065E and N145E (Fig. 3).

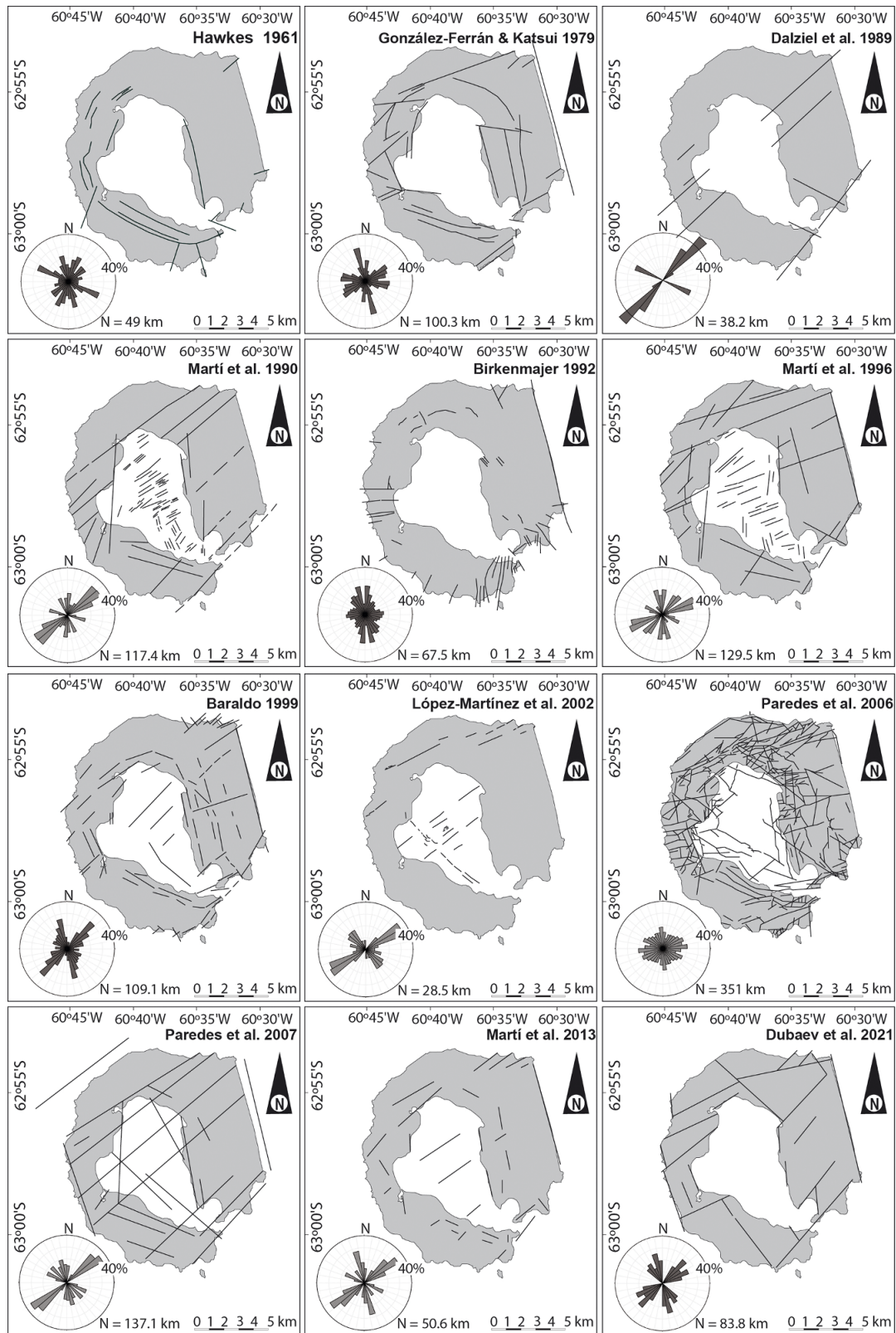


Figure 3. Separate mapping of the lineaments proposed by the 12 different papers analysed in this study, obtained from aerial photography, satellite images, digital terrain models and field data. The rose diagrams show the length-weighted orientations of the lineaments represented. The outer circle represents 40% of the data and N indicates the total length of the data.

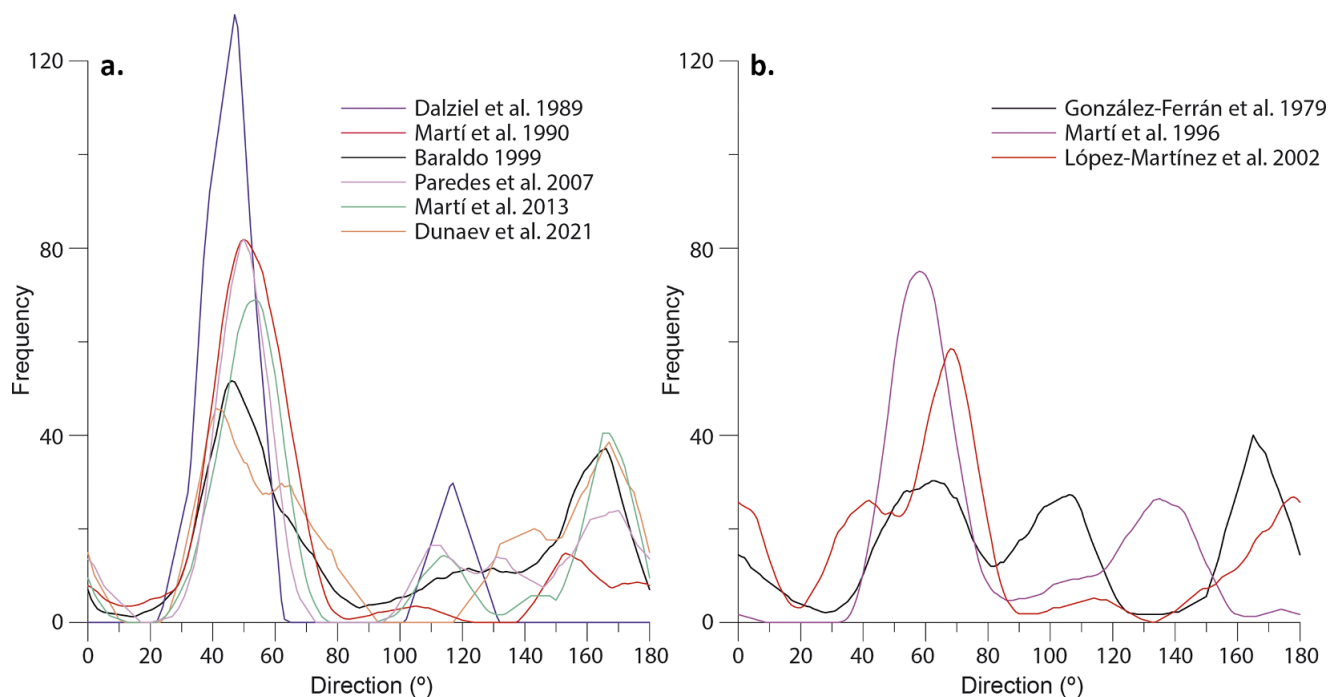


Figure 4. Smoothed frequency curves showing the orientation of the lineaments identified on Deception Island by **a.** Dalziel *et al.* (1989), Martí *et al.* (1990), Baraldo (1999), Paredes *et al.* (2007), Martí *et al.* (2013) and Dunaev *et al.* (2021) and **b.** González-Ferrán *et al.* (1970), Martí *et al.* (1996) and López-Martínez *et al.* (2002).

From a visual point of view, it is possible to compare the different frequency curves representing the orientations of lineaments determined by the various authors analysed in this study. As previously mentioned, these lineaments have been defined based on geological observations and fracture data collected from rock outcrops on the island, as well as from interpretations of satellite images, aerial photographs and digital elevation models. It has been observed that, although in general the mapped lineaments do not exactly coincide in the same locations (see Figs 2 & 3), there are some matches in the orientations defined by the various authors who mapped them. The lineaments defined by Dalziel *et al.* (1989), Martí *et al.* (1990, 2013), Baraldo (1999), Paredes *et al.* (2007) and Dunaev *et al.* (2021) present similar directional distributions, although with variations in frequencies, showing a primary orientation with a mean value of N050E, and two secondary orientations, N115E and N165E (Fig. 4a). However, the rest of the lineament maps analysed exhibit different orientation patterns, with González-Ferrán & Katsui (1970), Martí *et al.* (1996) and López-Martínez *et al.* (2000) showing only a common main orientation of approximately N060E (Fig. 4b).

The data obtained from the application of Spearman's correlation to compare the weighted curves generally show weak correlations between them (see Table I), with only the relationships between the lineament directions identified by Martí *et al.* (1990, 2013), Baraldo (1999), Paredes *et al.* (2007) and Dunaev *et al.* (2021) showing very strong correlation values, thus corroborating the visual analysis of the frequency curves. Strong correlation values were also obtained between the lineaments defined by Baraldo (1999) with Martí *et al.* (1990) and López-Martínez *et al.* (2000); Dunaev *et al.* (2021) with Paredes *et al.* (2007); and González-Ferrán & Katsui (1970) with Paredes *et al.* (2006) and Martí *et al.* (2013) (Table I). Finally, moderate correlations were found between the orientations of the lineaments defined by Baraldo (1999) with González-Ferrán & Katsui (1970), Dalziel *et al.*

(1989) and Martí *et al.* (1996); Dalziel *et al.* (1989) with Hawkes (1961), López-Martínez *et al.* (2000) and Paredes *et al.* (2007); and Dunaev *et al.* (2021) with González-Ferrán & Katsui (1970) and López-Martínez *et al.* (2000) (Table I).

From the analysis of geophysical data obtained on the island, the existence of linear structures has also been determined. Gravimetric surveys conducted in Port Foster (Carbó *et al.* 2001, Navarro *et al.* 2002, Muñoz-Martín *et al.* 2005) show an anomaly pattern with a NE-SW-orientated axis of minimum gravimetric values, bounded to the south and north by two axes of positive gravimetric anomalies. These elongated anomalies are further intersected by another NE-SW axis of minimum gravimetric values. Based on this distribution of anomalies, a number of fracturing directions have been inferred, showing three preferred orientations (Fig. 5a): 1) NW-SE, between Punta Murature and the southern part of Fumarole Bay, from the eastern part of Telefon Bay to Pendulum Cove and from northern Whalers Bay crossing the Neptunes Bellows, 2) NE-SW, from Punta Murature to the northern sector of Pendulum Cove, south of Fumarole Bay, along both margins of Irizar Lake and from the coastal area in front of Mount Kirkwood to Ronald Hill, and 3) N-S, from Punta Murature to Telefon Ridge. From the study of magnetic anomalies (Muñoz-Martín *et al.* 2005, Catalán *et al.* 2014), a NE-SW maximum is observed north of the island, extending along the northern sector of Telefon Ridge, bounding the southern part of Kendall Terrace, to Macaroni Point (Fig. 5b). Pueyo *et al.* (2014) interpreted the existence of a series of tectonic features based on an anisotropy of magnetic susceptibility (AMS) study of samples collected from various post-caldera units of Deception Island. This study determined that the AMS values are not compatible with the tilting of the emplacement surface of the volcanic flows. This incompatibility can be resolved through tilting processes related to caldera collapse and non-coaxial tilting relative to the emplacement surface, associated with tilting directions compatible with the tectonic regime of the island. This AMS

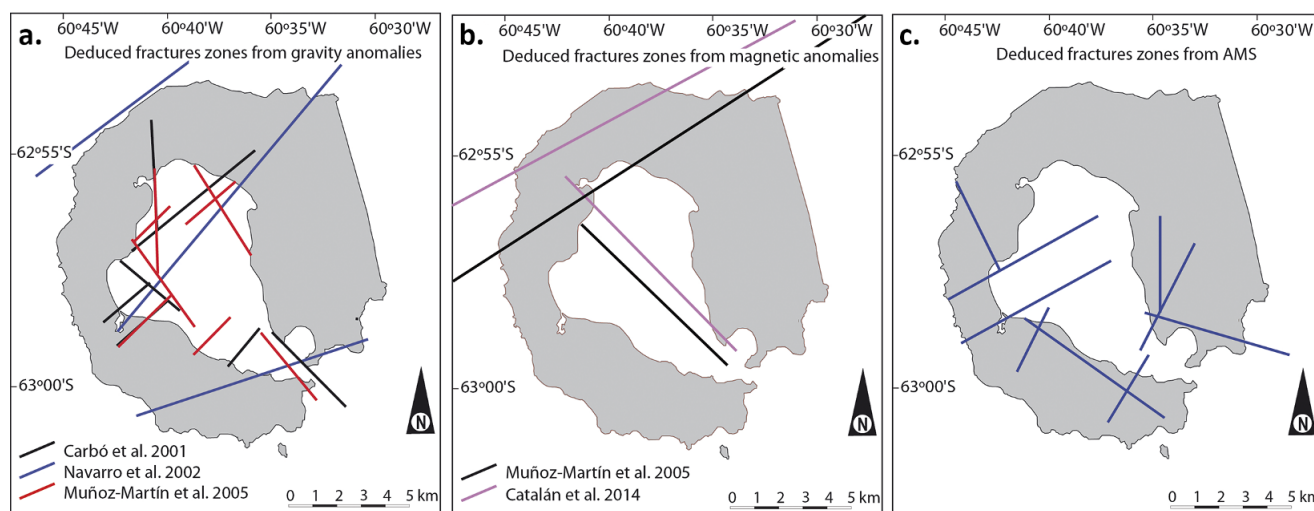


Figure 5. Mapping of fracture zones interpreted from **a.** Bouguer gravity anomalies (Carbó *et al.* 2001, Navarro *et al.* 2002, Muñoz-Martín *et al.* 2005), **b.** magnetic anomalies (Muñoz-Martín *et al.* 2005, Catalán *et al.* 2014) and **c.** tilting of volcanic units established from anisotropy of magnetic susceptibility (AMS) analysis (Pueyo *et al.* 2014).

analysis has enabled the detection of both tilted volcanic units and areas of the island unaffected by post-emplacement tilting. A series of faults responsible for these tilting processes, which are not currently observable because they are covered by more recent volcanic deposits, have been defined. NE-SW structures have been identified, bounding the northern and southern sectors of Fumarole Bay and extending towards Pendulum Cove, near Gabriel de Castilla Base (Spain), and from Collins Point to Ronald Hill and the crest of Mount Pond, with a NW-SE direction from Punta Murature to the northern coast of the island, parallel to the crest of Mount Kirkwood near the coast of Port Foster, and from South East Point to Ronald Point. A N-S-orientated fault from Ronald Hill to Crimson Hill is also described (Fig. 5c).

Based on reflection seismic surveys conducted in 1987–1988 and 1988–1989 applying Geopulse and Sparker acquisition systems, the main tectonic structures affecting the fill units of Port Foster were characterized (Rey *et al.* 1990, 1992, 1995, 2002). These studies determined the existence of an extensional fault with a NE-SW orientation, located between Fumarole Bay and Pendulum Cove, which presents a displacement of ~250 m. Parallel to this structure, a set of conjugate normal faults develop, affecting the most recent depositional units, giving the bay a horsts and grabens structure. Rey *et al.* (1992) and López-Martínez *et al.* (2000) mapped another NW-SE normal fault, sub-perpendicular to the main structure, located in the western part of Port Foster, extending from Punta Murature to the vicinity of Collins Point.

Finally, studies focused on the geochemistry of bottom sediments and surface waters (0.5–1.0 m depth) in Port Foster have found evidence of the distribution of certain elements following very defined trends, which these authors relate to the existence of volcanic cones, mounds and vents formed in association with normal extensional faults that facilitate the ascent of hydrothermal fluids enriched in these elements. Rey *et al.* (1997, 2002) and Somoza *et al.* (2004) show a preferred distribution on the seafloor, with sediments rich in Mn, Fe and Eu distributed in a NW-SE direction from Punta Murature to Collins Point, and those with high As and Ba contents distributed in a NE-SW direction from Fumarole Bay to the north of Pendulum Cove. Belyaev *et al.* (2024) measured trace metals, greenhouse gases and inorganic nutrients in the surface waters of Port Foster during January–February 2021.

This study, despite lacking a uniform sampling distribution across Port Foster's surface, shows a certain trend in the distribution of the analysed nutrients (NO_3^- and NH_4^+), exhibiting a NE-SW orientation. NO_3^- shows a preferred distribution from the coast near Gabriel de Castilla Base (Spain) to the vicinity of Ronald Hill, whereas NH_4^+ extends from east to west of Telefon Bay, from Cross Hill to the north of Pendulum Cove. These authors suggest that these nutrients are products of biochemical processes related to hydrothermal inputs.

Fracturing analysis

The fracturing data regarding the volcanic rocks of Deception Island were obtained during four field campaigns carried out in 2001 (Maestro *et al.* 2007) and in 2004, 2005 and 2007 (Paredes *et al.* 2006, Pérez-López *et al.* 2007, 2008). A total of 27 measurement stations were assessed, with six located in pre-caldera units and the rest in post-caldera units (Fig. 6). A total of 673 fracture planes were measured, of which 450 are faults, 190 are joints and 33 are basaltic dykes (Fig. 7). In general, these fractures exhibit dips ranging from 7° to 90°, with a modal value of 84° and a mean value of 72°. The fractures measured in the field display a somewhat radial distribution, although two sub-perpendicular preferred directions, N020E and N128E, are in evidence (Fig. 8a). Additionally, considering the fracture directions measured at each of the stations, there is significant heterogeneity in the preferred orientations between stations, with no constant preferred direction recurring across all of them, even at stations that are relatively close to one another (e.g. stations 13, 14, 15, 16, 17, 18, 19 and 20).

Regarding the different types of fracture planes, the faults exhibit centimetre- to metre-scale displacements, primarily with a normal component (347 faults), followed by faults with a reverse component (86 faults) and strike-slip faults (17 faults). These exhibit two preferred directions: N015E and N128E (Fig. 8b). The normal faults have dips ranging from 7° to 89°, with a modal value of 85° and a mean value of 71°. Their orientations are N015E, N060E and N130E (Fig. 8b). The reverse faults have dips ranging from 11° to 90°, with a modal value of 45° and a mean value of 62°. They exhibit two main orientations, N040E and N118E, and two secondary orientations, N095E and N150E (Fig. 8b). The

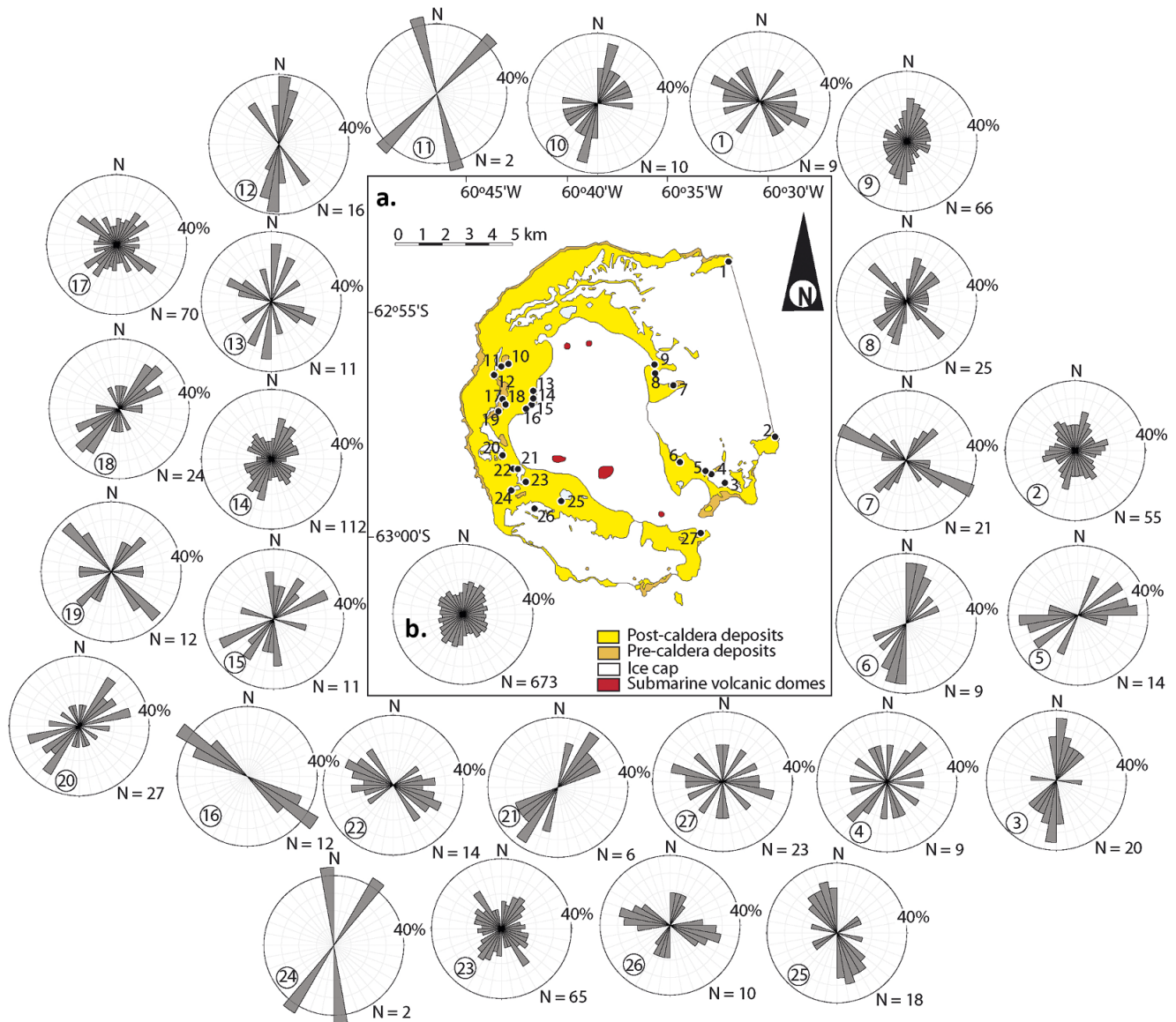


Figure 6. **a.** Simplified geological sketch map of Deception Island (modified from Smellie & López-Martínez 2000, Smellie 2001) and locations of the fracture sites. Rose diagrams show the orientation of fractures at the outcrop scale (outer circle represents 40%). N is the number of fractures measured at each site. **b.** Rose diagrams indicating the orientation frequency for all measured fractures.

strike-slip faults (9 sinistral and 8 dextral) have dips ranging from 55° to 89° , with a modal value of 88° and a mean value of 81° . Their main orientation is N010E, with two secondary orientations, N040E and N110E (Fig. 8b). The joints exhibit dips ranging from 25° to 90° , with a modal value of 89° and a mean value of 75° . The main orientation is N032E, with three secondary directions, N078E, N098E and N135E (Fig. 8c). Finally, the dykes, which have thicknesses ranging from centimetres to metres, exhibit dips between 69° and 88° , with a modal value of 84° and a mean value of 80° . Their main direction is N035E, with two secondary orientations, N075E and N163E (Fig. 8d).

Visual analysis of the frequency curves of the different types of fractures analysed indicates a certain similarity in some of the fracture directions (Fig. 8). A correlation can be observed between the orientations of dykes and joints at approximately N040E, N078E and N098E, whereas no similarity is found between the orientations of these structures and the faults in general. However, when

dividing the faults into different types based on their sense of motion (normal, reverse and strike-slip faults), a relationship is noted in the preferred direction of the normal and dextral faults orientated at N010E and the dykes, joints and reverse and sinistral faults orientated at N040E (Fig. 8). When analysing the values obtained by applying Spearman's correlation to the frequency curves of the differentiated fracture types (Table I), it is observed that dykes and sinistral faults show a very strong correlation, that diaclasses and reverse faults, as well as normal faults and dextral faults, show strong correlations and that diaclasses, dykes and sinistral faults show a moderate correlation.

Relationship between fracture directions measured in the field and identified lineaments

A correlation analysis has also been carried out to determine the relationship between the frequency curves of directions of

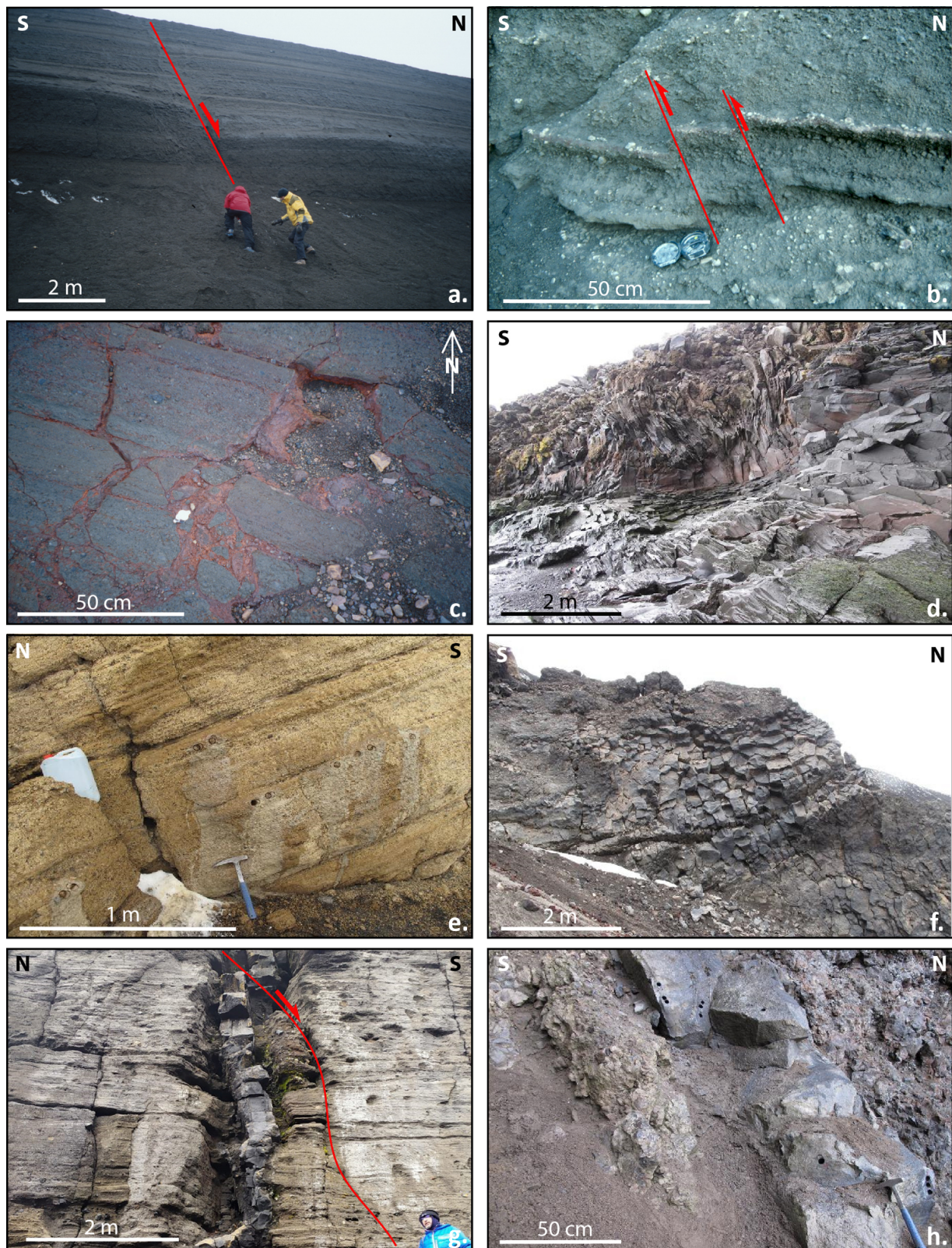


Figure 7. Examples of the different types of fractures affecting the volcanic units of Deception Island. **a.** Normal fault affecting the pyroclastic deposits of the Pendulum Cove Formation in the vicinity of Punta Murature. **b.** Reverse faults affecting the Pendulum Cove Formation units north of Punta Murature. **c.** Joints with mineralization in the Pendulum Cove Formation north of Punta Murature. **d.** Joints affecting the Kendall Terrace Member units between Gabriel de Castilla Base and Collins Point. **e.** Joints affecting the Baily Head Formation units in the vicinity of Whalers Bay. **f.** Columnar disjunction affecting a dyke intruding Kendall Terrace Member units at Telefon Ridge. **g.** Dyke intruding into the Baily Head Formation units in the Irizar Lake area, later affected by a normal fault. **h.** Dyke affecting the Fumarole Bay Formation units in the Stonethrow Ridge area.

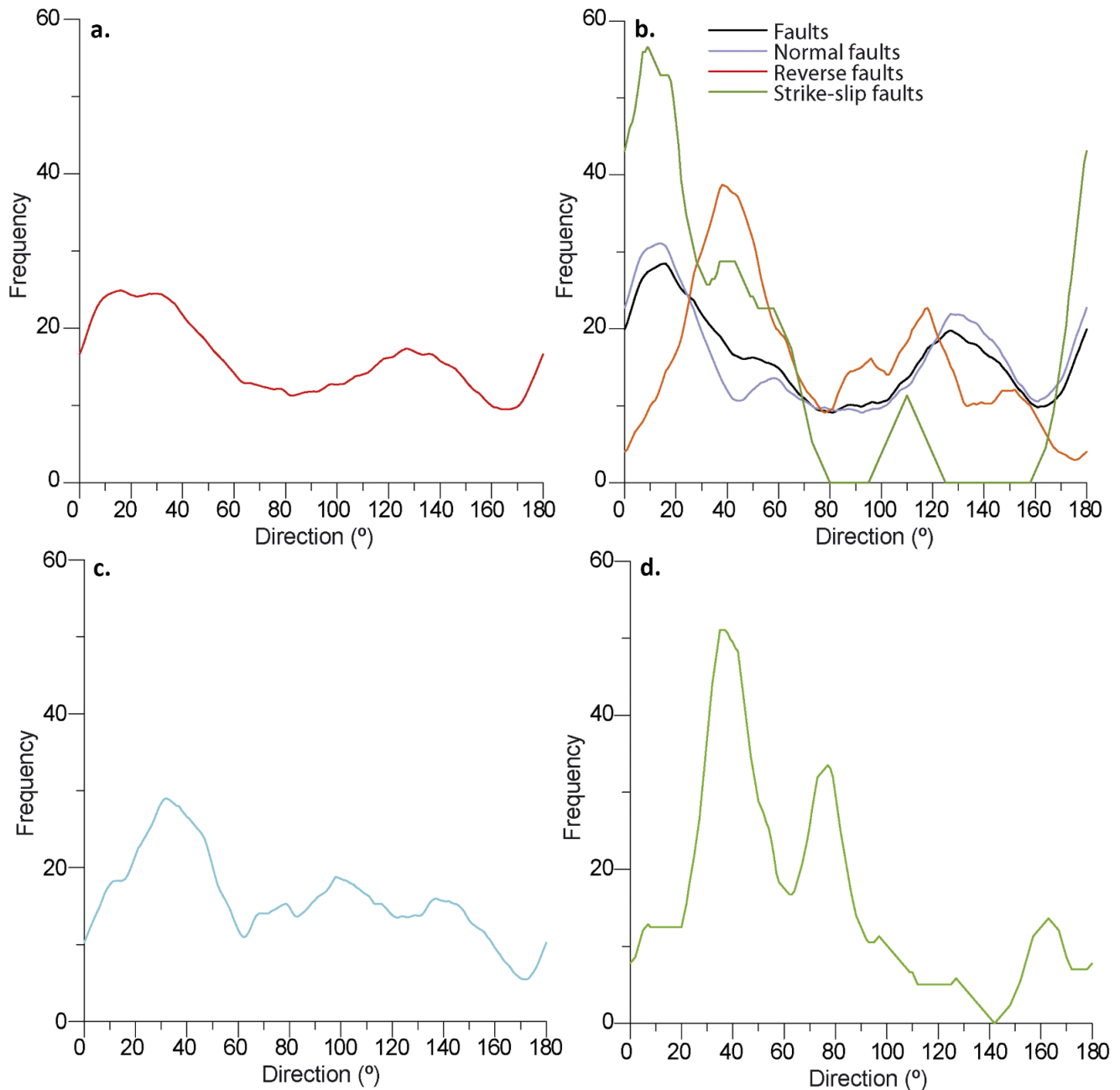


Figure 8. Smoothed frequency curves showing the orientation for all measured **a.** fractures, **b.** faults, **c.** joints and **d.** dykes.

the different types of fractures analysed (faults, joints and dykes) and the lineaments identified by the various authors considered in this study. Comparing the frequency curves obtained from the orientations of fractures measured in the field and the lineaments defined on Deception Island reveals no similarity, with maxima frequency values in fracture orientations corresponding to minima frequency values in lineament orientations (Fig. 9).

The Spearman's correlation values between the fractures and the lineaments show no or weak correlation, or, in several cases, even negative correlation (Table I). Considering only the positive correlation indices with moderate to very strong correlation strength, it can be observed that there is a very strong correlation between

the directions of reverse faults and the orientations of lineaments proposed by Dalziel *et al.* (1989) and between the sinistral faults and lineaments mapped by Martí *et al.* (1990) (Table I). Strong correlations are found between the directions of the dykes and the lineaments mapped by Martí *et al.* (1990, 1996), as well as between the directions of the sinistral faults and the lineaments identified by Martí *et al.* (1996) (Table I). Finally, moderate correlations exist between the orientations of the joints and the lineaments mapped by Dalziel *et al.* (1989), between the directions of the dykes and the lineaments proposed by Dalziel *et al.* (1989) and Dunaev *et al.* (2021), between the orientations of reverse faults and the lineaments identified by Hawkes (1961) and between the directions of sinistral faults and the lineaments mapped by Hawkes (1961),

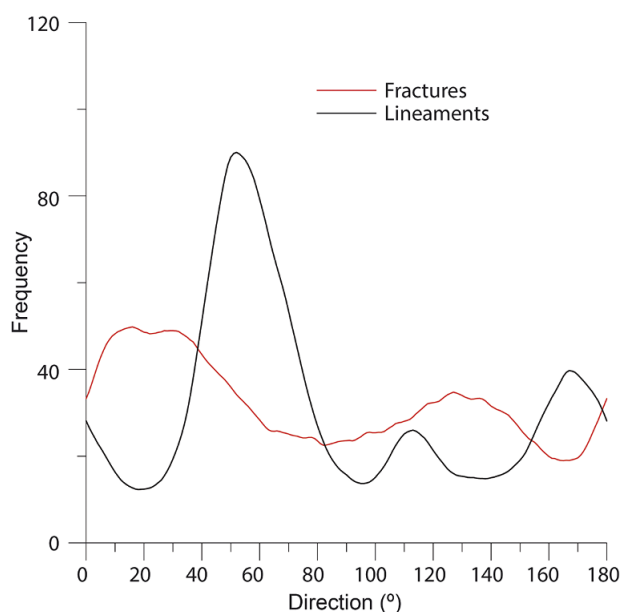


Figure 9. Smoothed frequency curves showing the orientation of all lineaments and fractures measured in rock outcrops on Deception Island published by the various authors analysed in this study.

Dalziel *et al.* (1989), Martí *et al.* (2013), Paredes *et al.* (2007) and Dunaev *et al.* (2021) (Table 1).

Distribution of heated ground, fumaroles, volcanic edifices and earthquake epicentres

Hydrothermal flows originating from volcanic processes are channelled to the surface through fractures. Evidence of these flows includes the development of heated ground and fumaroles on the surface, which are therefore preferentially located along fractures. On Deception Island, a series of specific areas showing the presence of these thermal anomalies, catalogued as fumaroles, evidence of fumarolic activity and heated ground, have been mapped in the same way by López-Martínez *et al.* (2000) and Smellie & López-Martínez (2000). A total of 38 such locations have been identified, primarily distributed along the coast of the island's inner bay, mainly in the areas of Fumarole Bay, Punta Murature, Telefon Bay, Pendulum Cove and Whalers Bay (Figs 10a & 11). Thermal anomalies have also been observed in some sectors of the glacier cap that covers the eastern flank of the island, north-east of Ronald Hill and north of Mount Pond (Fig. 10a). It is possible that such thermal anomalies may exist in other places, but the thick ice cover, as mentioned earlier, which extends mainly over the eastern and south-western sectors of the island, prevents their observation. Additionally, the analysis includes thermal anomaly data from the sea surface in Port Foster, obtained in December 2000 during the HYDRODEC-2000 cruise (Somoza *et al.* 2004), when temperatures up to 17°C were detected (Fig. 10a). Similar sea-surface thermal anomalies were observed by Dykes *et al.* (2001) in the same area in November 2000, where temperatures between 7°C and 15°C were recorded. The distribution of these thermal anomaly zones shows a preferred NE-SW orientation, extending from Fumarole Bay to Pendulum Cove (Fig. 10a). Additionally, two N-S-orientated alignments can be distinguished, one extending from Punta Murature up to the north of Cross Hill and the other extending from the

central part of Port Foster up to the north of Telefon Bay, as well as an E-W orientation from Pendulum Cove to the glacier ridge north of Mount Pond and a NW-SE orientation from Ronald Hill up to Whalers Bay (Fig. 10a).

Furthermore, the construction and development of volcanic edifices are generally associated with the expulsion of magma through structural discontinuities in the upper crust. Magma migration is controlled by changes in the stress field related to tectonic processes, and it occurs along fractures or crustal discontinuities (Delaney *et al.* 1986, Dahm 2000, Gudmundsson & Philipp 2006, Gaffney *et al.* 2007, Pedrera *et al.* 2011, Rivalta *et al.* 2015). The monogenetic volcanoes that developed after the caldera collapse on the emerged part of Deception Island and in the Port Foster area have been mapped based on works by López-Martínez *et al.* (2000), Smellie & López-Martínez (2000) and Pedrazzi *et al.* (2020) (Fig. 10b). Additionally, the submarine volcanic morphologies around Deception Island identified in publications by Barclay *et al.* (2009) and Geyer *et al.* (2021) have been mapped (Fig. 10b). A total of 260 monogenetic volcanic morphologies have been distinguished, some of which are well preserved, while others have been inferred (Fig. 12). Some of these inferred morphologies, as previously mentioned in the 'Data and methodology of the structural analysis' section, are subglacial circular depressions that affect the glacier located on the eastern flank of the main volcanic cone constituting the island (López-Martínez *et al.* 2000). The distribution of volcanic edifices shows a preferred N060E orientation, which extends both in the submerged area around the island and in the emerged zone, arranged along two parallel lineaments (Fig. 10b). The southernmost lineament extends from the western sector of Bransfield Basin through New Rock Island, reaching Crater Lake, passing through the Stanley Patch volcanic edifice, continuing to Mount Pond and extending once again to the eastern sector of Bransfield Basin. The second lineament is located further north, extending from the western sector of Bransfield Basin, passing along the northern coast of Telefon Bay and continuing through Goddard Hill to the eastern sector of Bransfield Basin. A NW-SE trend is also observed along the crest of Mount Kirkwood, as well as two N-S alignments, one along the eastern coast of Port Foster, from Kroner Lake to Crimson Hill, and the other to the east of Mount Pond crest.

Volcano-tectonic earthquakes are caused by shear or tensile fractures during magma movement from depth to the Earth's surface through conduits and dykes (Zobin 2014). These earthquakes occur within and around the volcanic edifice and reflect the interaction of two general geological processes: magma migration towards the surface from the crustal and mantle magmatic reservoirs and tectonic activity in the crust. The alignment of earthquake epicentres helps us to define the trace of the faults that generated them. A total of 1561 epicentres have been located on Deception Island and its nearby surroundings between 1999, 2009–2020 and 2022–2024, as recorded by the Andalusian Institute of Geophysics (University of Granada) and the IGN (Fig. 10c). These earthquakes are of low magnitude, with a maximum value of 3.0 and a modal value of 1.4. Due to their low magnitude and the fact that a one-dimensional velocity model was used to determine their depth, there is significant uncertainty in their depth estimation, with most hypocentres being shallow, located within the first 3 km of the crust. The epicentres are widely distributed across the island, but they are primarily concentrated along an axis running mainly west to east across the island from Fumarole Bay to Mount Pond, with an orientation of N070E (Fig. 10c).

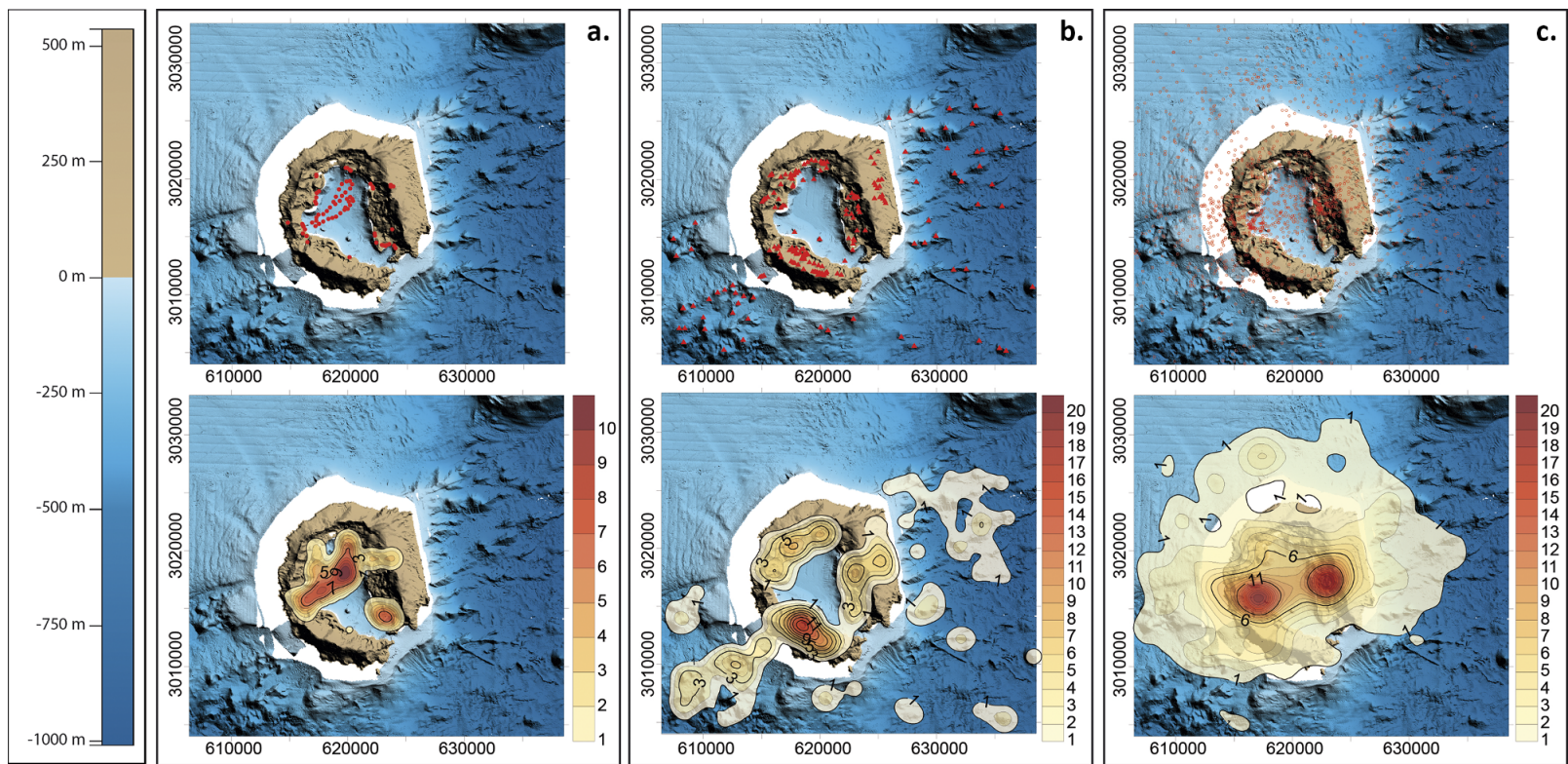


Figure 10. Distribution maps of areas of **a.** thermal anomalies (heated ground and fumaroles) (López-Martínez *et al.* 2000, Smellie & López-Martínez 2000, Somoza *et al.* 2004), **b.** central zone of well-preserved and inferred volcanic edifices (López-Martínez *et al.* 2000, Smellie & López-Martínez 2000, Barclay *et al.* 2009, Pedrazzi *et al.* 2020, Geyer *et al.* 2021) and **c.** earthquake epicentres (Andalusian Institute of Geophysics, University of Granada and IGN, 1999, 2009–2020 and 2022–2024). Contour maps of the density of these elements have also been made. The isoline values represent the density calculated as the number of elements per square kilometre using a two-dimensional and symmetric Gaussian kernel density method.

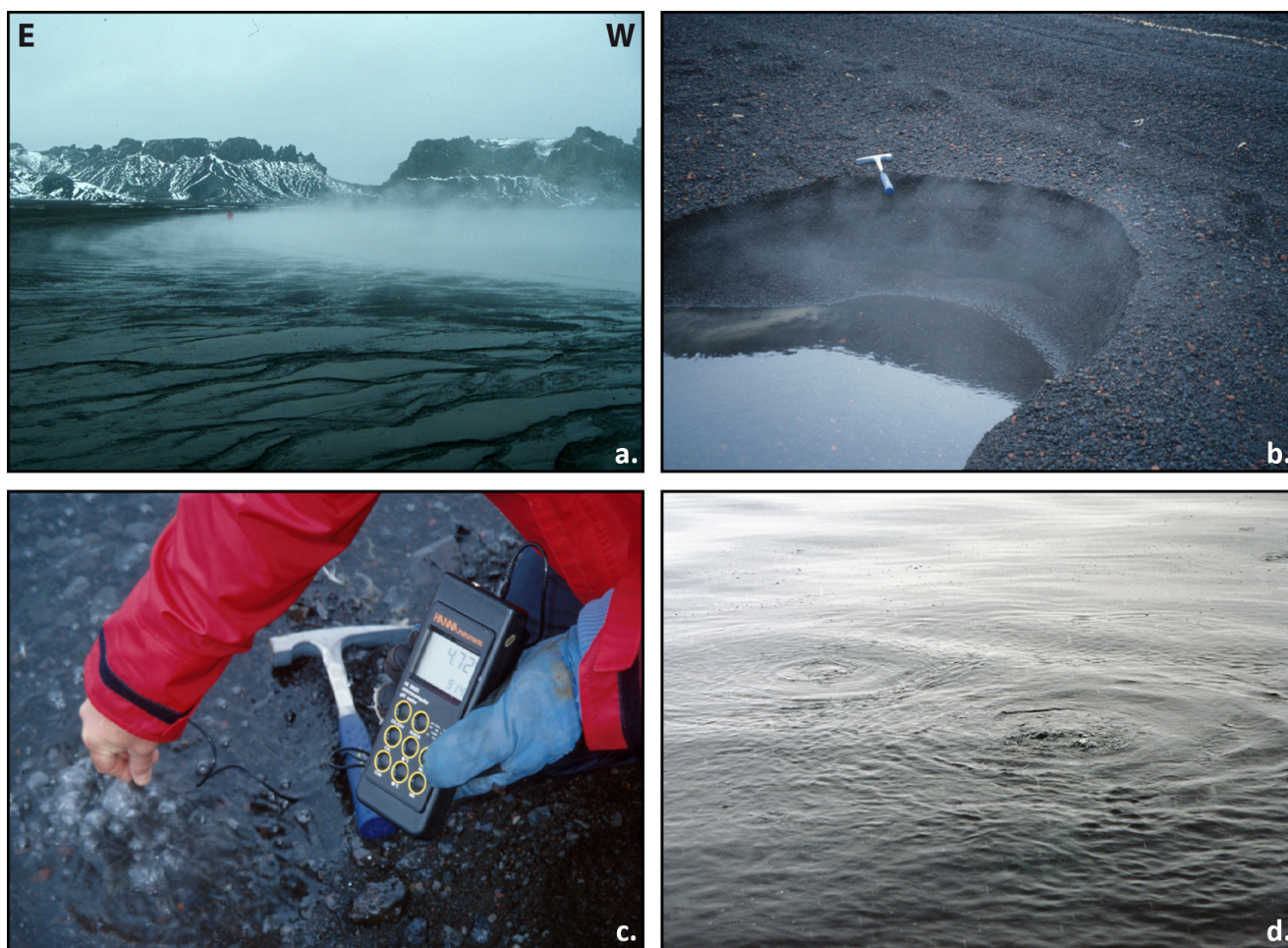


Figure 11. Examples of different areas where thermal anomalies are evident on Deception Island: **a.** fumaroles on Whalers Bay beach; **b.** fumaroles on Pendulum Cove beach; **c.** temperature measurement on heated ground in the Fumarole Bay area; and **d.** bubbles in the water column in the Fumarole Bay area related to heated seepages.

Discussion

Correlation between the lineaments identified by various authors

Looking at the set of analysed pairs of variables corresponding to the directions defined by the various authors studied, only 10% show very strong correlation values. Considering the studies with a very strong correlation value (Martí *et al.* 1990, 2013, Baraldo 1999, Paredes *et al.* 2007, Dunaev *et al.* 2021), it can be determined that these authors relied on similar morphological features to establish the lineaments. They coincided in the methods and approaches used in their analyses, as morphometric data obtained from topographical analysis and aerial and satellite image processing predominated over field-based mapping of tectonic structures. The cases studied that present a strong to moderate correlation suggest a general tendency in which certain lineament directions tend to correlate due to their similarity; however, not all defined orientations show such similarity. It is especially noteworthy that the lineament directions defined by Birkenmajer (1992) do not correlate with the lineaments mapped by the other authors, as almost all correlation values obtained were negative (Table I). This may suggest that this study takes a very different geological approach or analyses different variables from the other studies.

The lineaments mapped by the various authors analysed show, in general, only a low number of very strong correlations. This suggests that there are other factors - not only geological - that influence the directions of the lineaments established by the various authors. These factors include personal interpretation, image resolution (which may limit or affect the perception of geological details), image scale (which affects the amount of visible information), prior knowledge of the geological context of the region and the use of data from previous studies (which can influence how lineaments are interpreted). Finally, there is the issue of the drawing criteria that each interpreter uses to define what constitutes a lineament, which may vary. Some authors may have focused only on observing fractures affecting rock units, whereas others may have included broader features such as lithological variations, coastlines, or lineations of volcanic cones. Other factors such as the environmental conditions of the analysed images (e.g. lighting and shadows) can also affect the perception of terrain features, influencing how lineaments are drawn. Cognitive biases such as prior prejudices or expectations can skew interpretations. The software used for visualization and analysis can also affect interpretation, and aesthetic aspects of the visual representation may influence how lineaments are presented, perhaps due to a prioritization of visual clarity over geological accuracy.

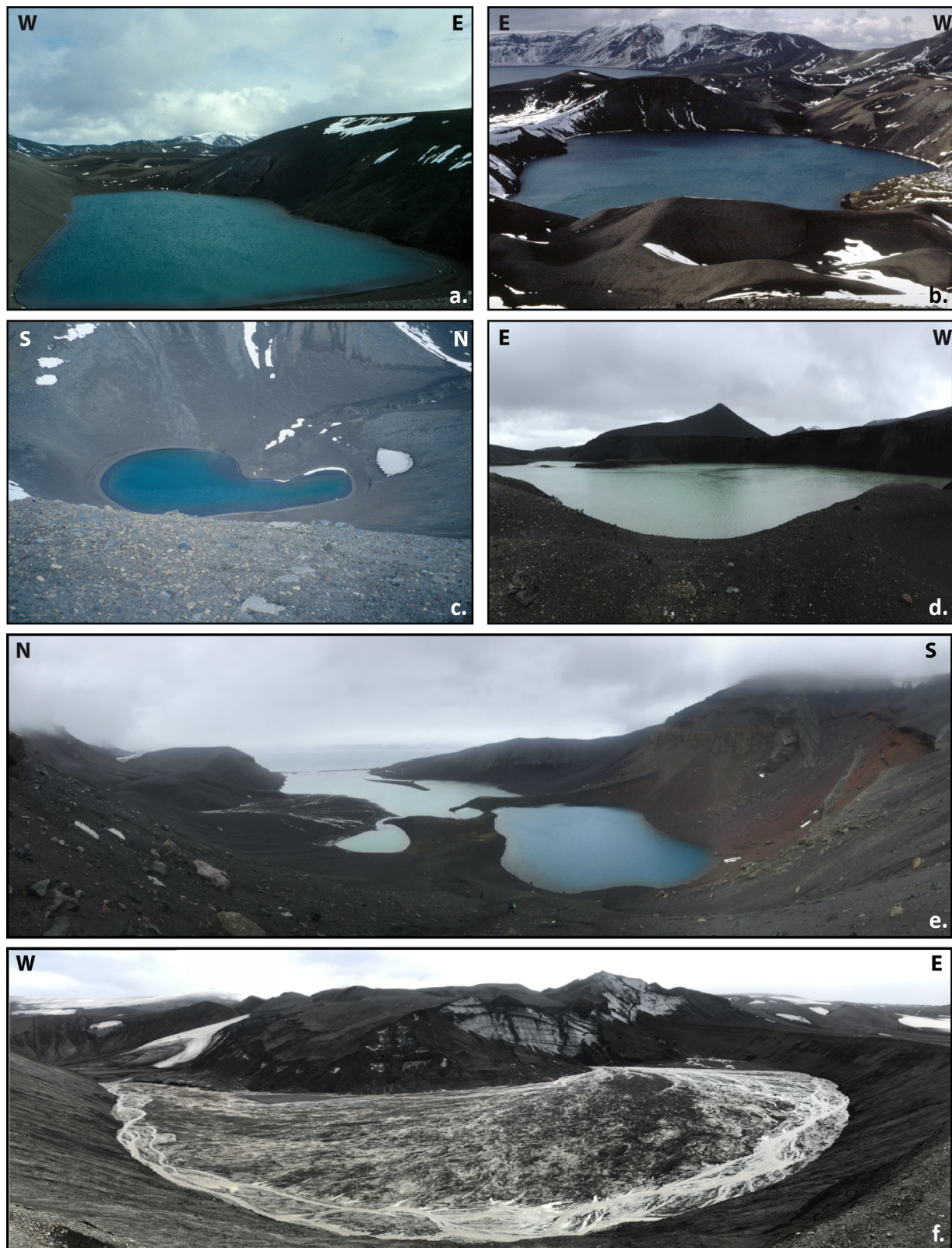


Figure 12. Examples of different well-preserved volcanic edifices on Deception Island: **a.** volcanic edifice south-east of Crater Lake; **b.** Crater Lake volcanic edifice; **c.** volcanic edifice north-west of Crater Lake; **d.** group of volcanic edifices around Irizar Lake; **e.** volcanic edifices west of Telefon Bay; and **f.** volcanic edifice east of Telefon Bay.

Origin and chronology of fractures in a volcanic setting

Fracture development within and around igneous intrusions is highly complex due to the formation mechanisms of these rocks. Three main types of fractures have been defined that may affect igneous rocks (Senger *et al.* 2015): 1) fractures developed by the emplacement of molten rock into the host rock, 2) post-emplacement fractures, affecting the intrusion and developed during the crystallization and rapid cooling process upon exposure, and 3) fractures unrelated to the intrusion, associated with tectonic stresses acting after the consolidation of the igneous rock.

Fractures developed during emplacement, also called 'inflation fractures' (Kattenhorn & Schaefer 2008), develop during the intrusion because the magma is over-pressurized when emplaced (Lister & Kerr 1991, Rubín 1995). This leads to the rupture of the host rock both on a local scale (Delaney & Pollard 1981, Delaney *et al.* 1986, Meriaux *et al.* 1999, Abdelmalak *et al.* 2012, Schofield *et al.* 2012, Galland & Scheibert 2013) and on a regional scale (Rubín & Pollard 1988, Jackson & Pollard 1990).

Post-emplacement fractures, also known as 'cooling fractures' (Kattenhorn & Schaefer 2008), form in intrusive rock due to thermal contraction during cooling (Hetényi *et al.* 2012). Magma cooling begins at the edges while the interior remains molten, generating stresses capable of creating joints as the rock solidifies. Many of the fracture sets generated under these cooling conditions tend to have a geometric relationship with the lines and planes of magmatic flow and are called 'primary fracture systems' (Balk 1937). In these cases, some are perpendicular to the flow; others are parallel to the flow planes; others are parallel to the flow planes but perpendicular to the edges of the magmatic body; some are oblique, arranged in shear planes; and, finally, some develop columnar structures.

Lastly, tectonic fractures form due to tectonic forces unrelated to the intrusion. These fractures may affect intrusive rocks (if the tectonic regime is post-emplacement) or the host rock (if the tectonic regime acts both before and after the emplacement). The stress field can generate new fracture planes, following a pattern determined by the rock's rheological properties, or reactivate pre-existing discontinuities, which is extremely common in rocks (Bott 1959, Jaeger 1960). As such discontinuities may adopt any spatial orientation, reactivated fractures do not necessarily form a system aligned with the symmetry of the stress axes.

Additionally, in our study area, the effects of regional-scale fracturing on Deception Island related to the volcanic edifice collapse process, which resulted in the formation of the caldera that defines the island's current morphology, must be considered. These fractures affect pre-caldera units. Caldera formation may result from crustal bulging due to inflation of a magma chamber or, conversely, from bulging due to deflation of a magma chamber (Holohan *et al.* 2005). Pre-caldera bulging due to chamber inflation generates a subordinate pattern of radial and concentric fractures. Radial fractures are extensional and propagate outward from the dome's centre, whereas associated concentric fractures initially form as inward-dipping reverse faults, although high stresses at the dome's summit may cause their reactivation with a normal component (Walter & Troll 2001). If the caldera originates from magma chamber deflation, the subsiding rock mass accommodates along concentric reverse, vertical or outward-dipping faults (Anderson 1936, Komuro 1987, Branney 1995, Acocella *et al.* 2000, Roche *et al.* 2000, Walter & Troll 2001). Radial faults do not form during this collapse. A concentric extension zone forms at the caldera's periphery and is accommodated by vertical- to inward-dipping normal faults. If

preceded by a dome phase, deflation-induced collapse leads to the closure of radial fractures, with possible reverse reactivation of inward-dipping dome-phase faults (Troll *et al.* 2002).

There are a wide range of fracturing mechanisms that have acted during the evolution of Deception Island and have overlapped throughout the geodynamic evolution of the island. Therefore, it is exceedingly difficult to discriminate between those fractures related to the processes of intrusion, cooling and consolidation from those of tectonic origin or due to the collapse of the volcanic edifice.

The preferred orientation of dykes and sinistral faults analysed in this study is consistent with the orientation of the main extensional structures defined in the Bransfield Basin (Gràcia *et al.* 1996, Lawver *et al.* 1996, Prieto *et al.* 1998). In some cases, these structures exhibit a certain sinistral motion component, reflected in the bathymetry, where an *en echelon* pattern and a slightly sigmoidal shape of the main volcanic ridges are observed. This is also consistent with a slight sinistral deformation component superimposed on the general normal extension of the basin (Gràcia *et al.* 1996). The preferred direction of the normal and reverse faults could be related to the extrusion mechanisms of volcanic rocks or could result from the collapse of the volcanic edifice. The sinistral and dextral movements of some structures may be related to the reactivation of reverse and normal faults and joints under the current NE-SW compressive stress field (González-Casado *et al.* 2000, Maestro *et al.* 2007, 2014, Pérez-López *et al.* 2007, 2008).

Lineations and their relationship with geomorphological features

In general, the delineation of lineaments is somewhat subjective, as has been shown in this study, and the lineament maps analysed differ in some cases from one interpreter to another in aspects such as orientation, location and dimension. Aspects related to the direction of the lineaments have been analysed in previous sections of this paper, both concerning the structural maps published by the various authors considered in this study and their relationship with the fracture data measured in the field. Differences in the location of the lineaments can be explained by considering factors such as the tone, texture and shading of the satellite images, aerial photographs or digital terrain models used for their determination, which may limit how accurately the physical reality is reproduced. Finally, the differences in the length of the drawn lineaments are more difficult to explain considering that, methodologically, the lineaments should be constrained to the area where they are clearly identifiable. Extrapolating their length beyond where they are observed should be avoided, as some of the lineaments analysed in this work, mapped by some authors, even extend to areas where there is no information, being covered by water.

As shown in Fig. 2 and previously discussed, when representing the lineaments identified on Deception Island by the various authors who have mapped them, they generally do not coincide geographically. However, it is possible to identify areas where their density and orientation are very similar, forming bands that, in some cases, can be related to major tectonic or volcanic morphological features. Fifteen linear features with lengths ranging from 3.6 to 14.3 km, which are common to several of the lineament maps studied (Fig. 13), have been identified as follows:

- Lineament 1, the eastern sectors of lineaments 2 and 3 and the central part of lineament 6 correlate with faults observed in the field and with major faults detected in high-resolution

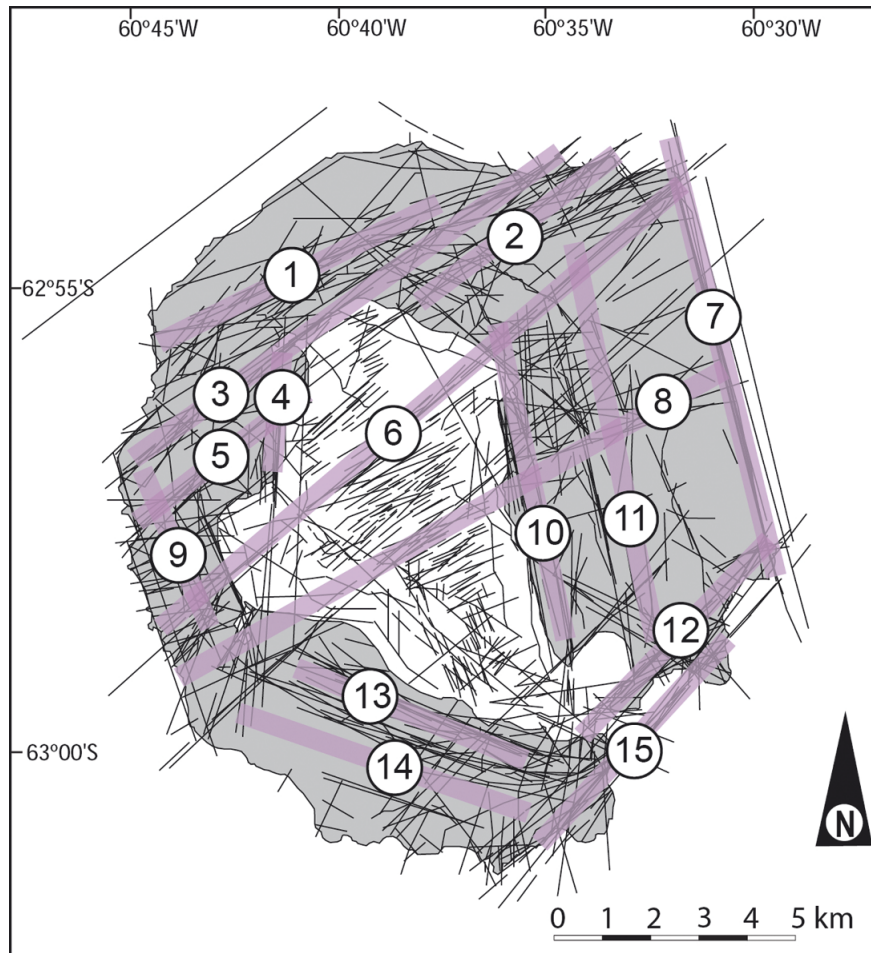


Figure 13. Synthesis of the most frequent lineament directions and their geographical locations based on the analysis of the cartography of the total number of lineaments proposed by the various authors analysed in this study.

off-shore seismic records within Port Foster (see Fig. 3; Rey *et al.* 1992, 2002, López-Martínez *et al.* 2000), as well as with one of the main trends defined by the gravimetric and magnetic anomalies described by Navarro *et al.* (2002) and Catalán *et al.* (2014) (Fig. 4), respectively. Furthermore, the main trends of the thermal anomalies are both on the emerged part of Deception Island and within Port Foster (López-Martínez *et al.* 1996, 2000, Somoza *et al.* 2004) (Fig. 8a), as well as regarding the distribution of Ba- and As-enriched sediments in Port Foster (Rey *et al.* 1997, 2002, Somoza *et al.* 2004). These lineaments have a NE-SW orientation and lengths ranging from 5.2 to 14.3 km.

- Lineament 4 is related to the orientation of a gravimetric anomaly identified by Carbó *et al.* (2001) and Muñoz-Martín *et al.* (2005) (Fig. 4a) and to one of the trends of thermal anomalies and volcanic edifices that extends from Murature Point to Cross Hill (Fig. 8a,b; López-Martínez *et al.* 2000). It has a NNE-SSW orientation and a length of 2.5 km.
- The central and western sectors of lineament 3 and lineaments 5, 8, 10 and 13 are associated with the orientation of a magnetic anomaly identified by Muñoz-Martín *et al.* (2005) (Fig. 4b), with the tectonic structures inferred from AMS tilt values, which imply tilting of the units (Fig. 4c; Pueyo *et al.* 2014), and with the distribution of volcanic edifices described on Deception Island on both the emerged and submerged parts (Fig. 8b; López-Martínez *et al.* 2000). Their orientations are NE-SW (lineaments

3, 5 and 8), NNW-SSE (lineament 10) and NE-SW (lineament 13), with lengths ranging from 4.4 to 13.1 km.

- Lineaments 1, 9, 11 and 14, the western sector of lineament 12 and the central sector of lineament 15 correspond to the main divide of Port Foster, which has a subcircular morphology throughout Deception Island and corresponds to the caldera rim (Fig. 1). Their dimensions range from 3.6 to 6.5 km.
- Lineament 7 is associated with the so-called Costa Recta on the eastern sector of Deception Island (Fig. 1). It has a length of 9.4 km, although the actual length of the coastline is 7.3 km, and it has a NNW-SSE orientation. The linear shape of the Costa Recta has traditionally been explained according to two hypotheses. The first refers to tectonic control (Rey *et al.* 1996, Pérez-López *et al.* 2004, Fernández-Ibáñez *et al.* 2005), whereby the rectilinear morphology of this sector is interpreted as the expression of the retreat of a scarp of a submarine fault with a normal component. The second hypothesis highlights the relevance of glacier and littoral dynamics (López-Martínez & Serrano 2002), proposing a balance between material supplied by the glacier and that removed by coastal dynamics. Based on existing bathymetric data (see Fig. 8; Barclay *et al.* 2009), no morphological features resembling a rectilinear scarp are observed in the submerged part of this sector that could indicate the presence of a normal fault. Furthermore, there is no evidence of the existence of such a fracture in the outcrops located at

both ends of the Costa Recta, at Macaroni Point and Baily Head, respectively. On the other hand, if we consider the oceanographical dynamics of the surface currents circulating in the Bransfield Basin, the presence of two currents has been described: the Transitional Zonal Water influenced by the Bellingshausen Sea and the Transitional Zonal Water influenced by the Weddell Sea (Tokarczyk 1987, García *et al.* 1994). The Transitional Zonal Water influenced by the Bellingshausen Sea occupies the northern part of the basin and propagates north-eastwards along the South Shetland Islands and passes south of Deception Island. Frey *et al.* (2023) identified the inflow of water between Deception and Livingston islands, coming from the Transitional Zonal Water influenced by the Bellingshausen Sea, which circulates parallel to the Costa Recta. Therefore, as proposed by López-Martínez & Serrano (2002), a probable explanation for this is that the linear shape of the Costa Recta results from a combination of glacier protection by two headlands resistant to erosion and marine erosion at the glacier front, rather than being a feature of tectonic origin.

- Lineament 8 is associated with the main structural trend where a significant number of epicentres are concentrated, as well as with faults observed in high-resolution seismic records obtained within Port Foster (Fig. 3; Rey *et al.* 1992, 2002, López-Martínez *et al.* 2000) and tectonic structures inferred from AMS tilt values, which imply tilting of the units (Fig. 4c; Pueyo *et al.*, 2014). It has a NE-SW orientation and a length of 13.1 km.

Lineaments showing evidence of tectonic and volcanic origin

Based on the above information, this study proposes a mapping of lineaments with clear evidence of geological significance, for which we have limited ourselves to identifying those elements that exhibit clear tectonic and/or volcanic control, restricting their length to what has been observed in field studies or inferred from geophysical data. These lineaments, sometimes with a curved morphology, have been grouped into three types: 1) tectonic origin, 2) volcanic origin related to the collapse of the main edifice of Deception Island and the development of the caldera and 3) volcanic origin related to the subsequent evolution of the caldera and the formation of secondary volcanic edifices (Fig. 14).

The lineaments of tectonic origin have a NE-SW orientation. They are mainly observed in the central and northern sectors of the emergent part of Deception Island, affecting the deposits that fill Port Foster. Their orientation is clearly related to the main structural trend that shapes the morphology of the Bransfield Basin, whose axis presents an orientation of N055–060E (Gràcia *et al.* 1996), locally intersected by transverse structures that act as transfer faults (N135–165E; Barker & Austin 1994, Prieto *et al.* 1998). These NE-SW-trending faults observed in the Bransfield Basin are primarily characterized by normal faulting (Gràcia *et al.* 1996), as evidenced by high-resolution seismic profiles in Port Foster (López-Martínez *et al.* 2000, Rey *et al.* 2002). However, considering the slightly sigmoidal shape of the main volcanic ridges east of Deception Island and the presence of small pull-apart basins, a minor component of left-lateral strike-slip deformation, superimposed on the general extensional regime of the basin, is also consistent (Gràcia *et al.* 1996). This left-lateral strike-slip component is manifested in the stepped morphology of the coastline observed in the north-eastern sector of Deception Island, around Macaroni Point, as well as in the areas of Goddard Hill and Mount Pond, where the trace of the Port Foster main divide is offset left laterally (Fig. 14; López-Martínez *et al.* 2000).

The boundary of the caldera structure, which developed following the collapse of the main edifice of Deception Island, defines a ring structure surrounding the entire island, marking the Port Foster main divide. This topographical boundary separates the subsided area from the undisturbed volcanic zone. Around this boundary, a series of faults can also be distinguished, distributed concentrically around the caldera boundary, delimiting the collapse in a stepped manner towards the caldera floor, with the flat central area representing the deepest part of Port Foster. These faults delimiting the collapse have served as conduits for magma and hot fluids to reach the surface, leading to the development of secondary volcanic edifices, with recent eruptions dated from the 18th century to 1970 (López-Martínez *et al.* 2002), and areas with fumaroles and heated ground. Three stepped levels produced by the collapse process can be distinguished: 1) the Port Foster main divide, extending along the island's highest areas, starting at Entrance Point and continuing through Mount Kirkwood, Vapour Col, Stonethrow Ridge, Telefon Ridge, Goddard Hill and Mount Pond and ending at Cathedral Crags, 2) the lineaments where the main secondary volcanic edifices, heated ground and fumaroles are located, extending through Collins Point, Irizar Lake, Fumarole Bay, Punta Murature, Cross Hill and the eastern sector of Telefon Bay and from Crimson Hill to Kroner Lake, and 3) a NW-SE-trending lineament in Port Foster, which is a normal fault with a dip plane towards the north-east, identified from the interpretation of high-resolution seismic profiles (López-Martínez *et al.* 2000, Rey *et al.* 1992, 2002), extending from Collins Point to Punta Murature, where several volcanic edifices have been identified (López-Martínez *et al.* 2000), including the one called Stanley Patch (Hopfenblatt *et al.* 2021).

Final remarks and conclusions

The identification and mapping of the significant morphostructural elements under tectonic and/or volcanic control and being supported by field observations and/or geophysical evidence may help to clarify the different existing proposals and contribute to future research efforts to improve the knowledge of the Deception Island volcano structure.

After a detailed review of the morphostructure of Deception Island based on both existing scientific literature and our own data, we analysed the various lineament maps and schemes created by different authors through the interpretation of aerial photographs, satellite images, digital terrain models and field measurements of brittle structures. Considering their direction and length, the lineaments determined on Deception Island exhibit three preferred directions: NE-SW, ESE-WSW and SSE-NNW. On the other hand, the fractures measured in the field generally show a radial distribution, although there are two preferred directions: NNE-SSW and SE-NW. Regarding the different types of fracture planes, the faults exhibit two preferred directions: NNE-SSW and SE-NW. The normal faults show NNE-SSW, NE-SW and SE-NW directions. The reverse faults exhibit two main orientations, NE-SW and ESE-WNW, and two secondary orientations, E-W and SE-NW. The strike-slip faults show a main N-S orientation, with two secondary orientations, NE-SW and ESE-WNW. The joints exhibit a main orientation, which is NE-SW, with three secondary directions, ENE-WSW, E-W and SE-NW. Finally, the dykes show a NE-SW main direction, with two secondary orientations, ENE-WSW and SE-NW.

This comparative study revealed significant disparities in the results obtained, with substantial differences in the location,

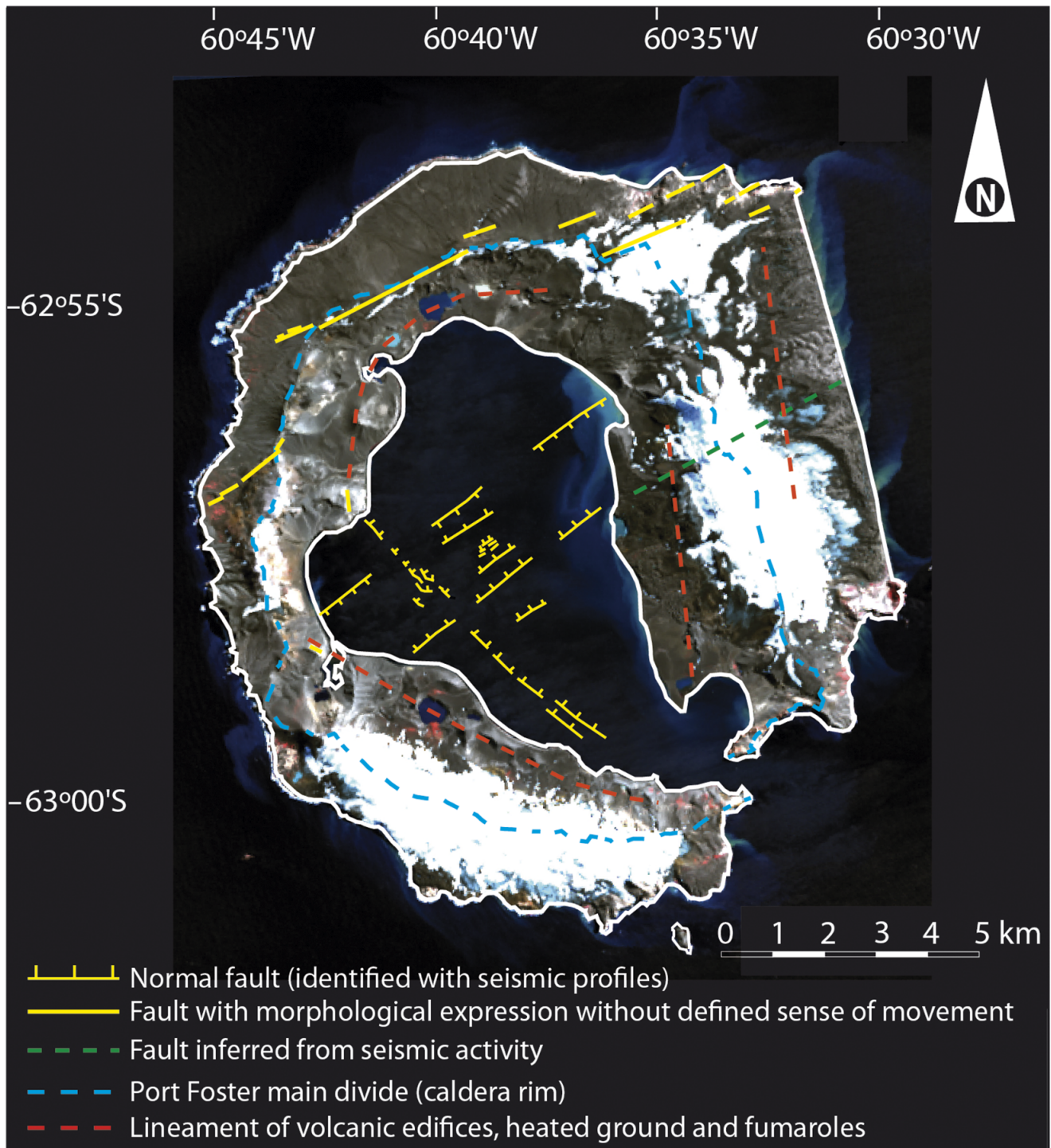


Figure 14. Proposed mapping of the lineaments on Deception Island based on morphological features clearly related to the tecto-volcanic activity of the island. Four types of morphostructural features have been defined: faults with morphological expression or inferred from indirect information (seismic activity), caldera boundaries and lineaments related to alignments of volcanic edifices, heated ground and fumaroles. Landsat 8 image of 20 February 2020 with 30 m spatial resolution.

direction and extent of the mapped lineaments. These differences may be attributed, among other factors, to subjective biases and the criteria used in personal interpretation, the resolution and scale of the images employed and the prior knowledge of the geological regional context.

Lineament analysis has proven to be a very useful tool for studying tectonic fracturing in many areas. The problem of applying this

methodology to volcanic islands is their complex evolution. The growth of volcanic islands is marked by a series of constructive episodes, such as the emplacement of molten rock in the host rock and the processes of crystallization and rapid cooling after exposure, as well as destructive ones, such as large-scale flank collapse, caldera collapse and fluvial and coastal erosion, which makes it difficult to establish a clear relationship between tectonic fracture

trends and the identified lineaments. Of course, this uncertainty is solved by carrying out field studies to determine which are the macroscale structures that define the lineaments, enabling us to determine their origin. For this purpose, we have used the detailed geological and geomorphological maps of Deception Island published by the British Antarctic Survey, which provide valuable context and help us to interpret the lineaments in relation to tectonic and volcanic structures (López-Martínez *et al.* 2000, Smellie & López-Martínez 2000).

Taking both factors into account and acknowledging that the previously existing lineament maps have often been used by other researchers in their work and served as the basis for their conclusions, we propose the coherency morphostructural map of Fig. 14, which represents elements with clear evidence of origin due to tecto-volcanic processes, based both on field observations and geophysical data. This morphostructural map shows the main lineaments, which generally show as straight lines but sometimes have a curved morphology, which are related to:

- i) *Tectonic origin*, with NE-SW and SE-NW orientation. The NE-SW-orientated lineaments correlate with the normal faults observed in the high-resolution seismic profiles obtained at Port Foster and with the one described in the Bransfield Basin, where it has been observed that they occasionally present a minor component of left-lateral strike-slip deformation. The SE-NW-orientated lineaments can be correlated with transverse structures described in the Bransfield Basin that act as transfer faults.
- ii) *Volcanic origin related to the collapse of Deception Island's main edifice and the development of the caldera*, defining a ring structure surrounding the entire island, marking the Port Foster main divide and a series of faults distributed concentrically, which have served as conduits for magma and hot fluids to reach the surface.
- iii) *Volcanic origin associated with the subsequent evolution of the caldera*, including the formation of secondary volcanic edifices, some of them from eruptions in historical times, the presence of thermal anomalies related to heated ground and fumaroles and a NW-SE-trending lineament in Port Foster, which is a normal fault with a dip plane towards the north-east, identified from the interpretation of high-resolution seismic profiles.

Acknowledgements. We thank E. Carmona and J. Almendros (IAG, University of Granada) and R. Abella (IGN, Madrid) for providing some geophysical data and J. Galindo and A. Pedrera for their insightful comments that helped to improve the quality of this paper. This work represents a contribution to the CSIC PTI, Polar Zone Observatory (PTI-POLARCSIC).

Financial support. This work has been funded in the framework of the Spanish Ministry of Science, Innovation and Universities projects TEMPERATE (PID2021-126495NB-C32) and GEOCHEM (PID2021-125778OB-I00).

Competing interests. The authors declare none.

Author contributions. All authors contributed to the design and implementation of the research, to the analysis of the results and to the writing of the manuscript.

References

- ABDELMALAK, M.M., MOURGUES, R., GALLAND, O. & BUREAU, D. 2012. Fracture mode analysis and related surface deformation during dyke intrusion: results from 2D experimental modelling. *Earth Planetary Science Letters*, **359**–360, 93–105.
- ACOCCELLA, V., CIFELLI, F. & FUNCIELLO, R. 2000. Analogue models of collapse calderas and resurgent domes. *Journal of Volcanology and Geothermal Research*, **104**, 81–96.
- ALMENDROS, J., IBÁÑEZ, J.M., ALGUACIL, G. & DEL PEZZO, E. 1999. Array analysis using circular wave-front geometry: an application to locate the nearby seismo-volcanic source. *Geophysical Journal International*, **136**, 159–170.
- ALMENDROS, J., CARMONA, E., JIMÉNEZ-MORALES, V., DÍAZ-MORENO, A. & LORENZO, F. 2018. Volcano-tectonic activity at Deception Island volcano following a seismic swarm in the Bransfield Rift (2014–2015). *Geophysical Research Letters*, **45**, 4788–4798.
- ALMENDROS, J., IBÁÑEZ, J.M., ALGUACIL, G., DEL PEZZO, E. & ORTIZ, R. 1997. Array tracking of the volcanic tremor source at Deception Island, Antarctica. *Geophysical Research Letters*, **24**, 3069–3072.
- ALMENDROS, J., WILCOCK, W., SOULE, D., TEIXIDÓ, T., VIZCAÍNO, L., ARDANAZ, O., *et al.* 2020. BRAVOSEIS: geophysical investigation of rifting and volcanism in the Bransfield Strait, Antarctica. *Journal of South American Earth Sciences*, **104**, 102834.
- ÁLVAREZ-VALERO, A.M., GISBERT, G., AULINAS, M., GEYER, A., KERESZTURI, G., POLO-SÁNCHEZ, A., *et al.* 2020. δD and $\delta^{18}O$ variations of the magmatic system beneath Deception Island volcano (Antarctica): implications for magma ascent and eruption forecasting. *Chemical Geology*, **542**, 119595.
- ANDERSON, E.M. 1936. The dynamics of the formation of cone sheets, ring dikes, and caudron subsidences. *Proceedings of the Royal Society of Edinburgh*, **56**, 128–163.
- ANTONIADES, D., GIRALT, S., GEYER, A., ÁLVAREZ-VALERO, A.M., PLA-RABES, S., GRANADOS, I., *et al.* 2018. The timing and widespread effects of the largest Holocene volcanic eruption in Antarctica. *Scientific Reports*, **8**, 17279.
- BALK, R. 1937. *Structural behavior of igneous rocks*. Geological Society of America Memoir, **5**, 177 pp.
- BARALDO, A. 1999. *Evolución geológica de la isla Decepción, islas Shetland del Sur, Antártida*. Doctoral thesis. Facultad de Ciencias Exactas y Naturales, Universidad de Buenos Aires, 213 pp.
- BARALDO, A. & RINALDI, C.A. 2000. Stratigraphy and structure of Deception Island, South Shetland Islands, Antarctica. *Journal of South American Earth Sciences*, **13**, 785–796.
- BARCLAY, A.H., WILCOCK, W.S.D. & IBÁÑEZ, J.M. 2009. Bathymetric constraints on the tectonic and volcanic evolution of Deception Island volcano, South Shetland Islands. *Antarctic Science*, **21**, 153–167.
- BARKER, D.H.N. & AUSTIN, J.A. JR. 1994. Crustal diapirism in Bransfield Strait, West Antarctica: evidence for distributed extension in marginal-basin formation. *Geology*, **22**, 657–660.
- BARKER, P.F. 1982. The Cenozoic subduction history of the Pacific margin of the Antarctic Peninsula: ridge crest-trench interactions. *Journal of the Geological Society*, **139**, 787–801.
- BARTOLINI, S., GEYER, A., MARTÍ, J., PEDRAZZI, D. & AGUIRRE-DÍAZ, G. 2014. Volcanic hazard on Deception Island (South Shetland Islands, Antarctica). *Journal of Volcanology and Geothermal Research*, **285**, 150–168.
- BELYAEV, O., HUERTAS, I.E., NAVARRO, G., AMAYA-VÍAS, S., DE LA PAZ, M., SPARAVENTI, E., *et al.* 2024. Hydrothermal alteration of seawater biogeochemistry in Deception Island (South Shetland Islands, Antarctica). *Frontiers in Marine Science*, **11**, 1432122.
- BERROCOSO, M., TORRECELLAS, C., JIGENA, B. & FERNÁNDEZ-ROS, A. 2012. Determination of geomorphological and volumetric variations in the 1970 land volcanic craters area (Deception Island, Antarctica) from 1968 using historical and current maps, remote sensing and GNSS. *Antarctic Science*, **24**, 367–376.
- BIRKENMAJER, K. 1992. Volcanic succession at Deception Island, West Antarctica: a revised lithostratigraphic standard. *Studia Geologica Polonica*, **101**, 27–82.
- BIRKENMAJER, K. 1995. Volcano-structural evolution of the Deception Island volcano, West Antarctica. *Terra Antarctica*, **2**, 33–40.
- BIRKENMAJER, K., SOLIANI, E. & KAWASHITA, K. 1990. Reliability of potassium-argon dating of Cretaceous–Tertiary island-arc volcanic suites of King George Island, South Shetland Islands (West Antarctica). *Zentralblatt für Geologie und Palaöntologie*, **1**, 127–140.
- BONATTO, A.L., BADI, G.A., BIDONE, A., CASELLI, A.T., BENGIOA, C.L. & IBÁÑEZ, J.M. 2007. Isla Decepción: Actividad sismovolcánica y localización de fuentes

- para los veranos 2003–2004 y 2004–2005. In *Actas del VI Simposio Argentino y III Latinoamericano sobre Investigaciones Antárticas*. Buenos Aires: Dirección Nacional del Antártico/Instituto Antártico Argentino, 1–4.
- BOTT, M.H.P. 1959. The mechanics of oblique slip faulting. *Geology Magazine*, **96**, 109–117.
- BRANNEY, M.J. 1995. Downsag and extension at calderas: new perspectives on collapse geometries from ice-melt, mining, and volcanic subsidence. *Bulletin of Volcanology*, **57**, 303–318.
- CARBÓ, A., MUÑOZ-MARTÍN, A., DÁVILA, J., CATALÁN, M. & GARCÍA, A. 2001. Análisis de nuevos datos gravimétricos marinos en el entorno de la Isla Decepción (Islas Shetland del Sur, Antártida). *Revista de la Sociedad Geológica de España*, **14**, 189–197.
- CARMONA, E., ALMENDROS, J., MARTÍN, R., SERRANO, I., STICH, D. & IBÁÑEZ, J.M. 2012. Results of seismic monitoring surveys of Deception Island volcano, Antarctica, from 1999–2011. *Antarctic Science*, **24**, 485–499.
- CARMONA, E., ALMENDROS, J., MARTÍN, R., CORTÉS, G., ALGUACIL, G., MORENO, J., *et al.* 2014. Advances in seismic monitoring at Deception Island volcano (Antarctica) since the International Polar Year. *Annals of Geophysics*, **57**, S50321.
- CASELLI, A.T., DOS SANTOS AFONSO, M. & AGUSTO, M.R. 2004. Gases Fumarólicos de Isla Decepción (Shetland Del Sur, Antártida): Variaciones químicas y depósitos vinculados a la crisis sísmica de 1999. *Revista de la Asociación Geológica Argentina*, **59**, 291–302.
- CASELLI, A.T., BADI, G., BONATTO, A.L., BENGUA, C.L., AGUSTO, M.R., BIDONE, A. & IBÁÑEZ, J. 2007. Actividad sísmica y composición química fumarólica anómala debido a posible efecto sello en el sistema volcánico, Isla Decepción (Antártida). *Revista de la Asociación Geológica Argentina*, **62**, 545–552.
- CATALÁN, M., MARTOS, Y.M., GALINDO-ZALDÍVAR, J. & FUNAKI, M. 2014. Monitoring the evolution of Deception Island volcano from magnetic anomaly data (South Shetland Islands, Antarctica). *Global Planetary Change*, **123**, 199–212.
- CAZABAT, C. 1975. Topologie ertsienne de la France. *Bulletin de la Société Française de Photogrammétrie*, **60**, 21–36.
- CHOK, N.S. 2010. *Pearson's versus Spearman's and Kendall's correlation coefficients for continuous data*. MSc thesis. University of Pittsburgh, 43 pp.
- CHUKWU-IKE, I.M. & NORWAN, J.W. 1977. Mineralized crustal failures show on satellite imagery of Nigeria. *Transactions of the Institution of Mining and Metallurgy*, **86**, 55–57.
- CORTÉS, A.L., MAESTRO, A., SORIANO, M.A. & CASAS, A.M. 1998. Lineaments and fracturing in the Neogene rocks of the Almazan Basin (N Spain). *Geological Magazine*, **135**, 255–268.
- CORTÉS, A.L., SORIANO, M.A., MAESTRO, A. & CASAS, A. 2003. The role of tectonic inheritance in the development of recent fracture systems, Duero Basin, Spain. *Internacional Journal Remote Sensing*, **24**, 4325–4345.
- DAHM, T. 2000. Numerical simulations of the propagation path and the arrest of fluid-filled fractures in the Earth. *Geophysical Journal International*, **141**, 623–638.
- DALZIEL, I.W.D., BIRKENMAJER, K., MPODOZIS, C., RAMOS, V.A. & THOMSON M.R.A. 1989. *Tectonics of the Scotia Arc, Antarctica*. Field Trip Guidebook, **180**. Washington, DC: American Geophysical Union, 206 pp.
- DAVIS, G.H. & REYNOLDS, S.J. 1996. *Structural geology of rocks and regions*. New York: Wiley, 776 pp.
- DELANEY, P.T. & POLLARD, D.D. 1981. *Deformation of host rocks and flow of magma during growth of minette dikes and breccia-bearing intrusions near Ship Rock, New Mexico*. US Geological Survey Professional Paper #1202. Washington, DC: US Geological Survey, 61 pp.
- DELANEY, P.T., POLLARD, D.D., ZIONY, J.I. & MCKEE, E.H. 1986. Field relations between dikes and joints: emplacement processes and paleostress analysis. *Journal Geophysical Research*, **91**, 4920–4938.
- DUNAIEV, N.N., BRYANTSEVA, G.V. & KUZNETSOV, M.A. 2021. The neotectonic structure of Deception Island (Antarctica) inferred from the results of structural and geomorphic analysis. *Doklady Earth Sciences*, **501**, 1001–1008.
- DYKES, K., STURZ, A. & GRAY, S.C. 2001. Investigation of hydrothermal activity at Deception Island, Antarctica. Presented at GSA Annual Meeting, 5–8 November, San Diego, CA, USA, Abstract 26270.
- FERNÁNDEZ-IBÁÑEZ, F., PÉREZ-LÓPEZ, R., MARTÍNEZ-DÍAZ, J.J., PAREDES, C., GINER-ROBLES, J.L., CASELLI, A.T. & IBÁÑEZ, J.M. 2005. Costa Recta beach, Deception Island, West Antarctica: a retreated scarp of a submarine fault? *Antarctic Science*, **17**, 418–426.
- FREY, D., KRECHIK, V., GORDEY, A., GLADYSHEV, S., CHURIN, D., DROZD, I., OSADCHIEV, A., *et al.* 2023. Austral summer circulation in the Bransfield Strait based on SADC measurements and satellite altimetry. *Frontiers in Marine Science*, **10**, 1111541.
- GAFFNEY, E.S., DAMJANAC, B. & VALANTINE, G.A. 2007. Localization of volcanic activity: 2. Effects of pre-existing structure. *Earth Planetary Science Letters*, **263**, 323–338.
- GALINDO-ZALDIVAR, J., JABALOY, A., MALDONADO, A. & SANZ DE GALDEANO, C. 1996. Continental fragmentation along the South Scotia Ridge transcurrent plate boundary (NE Antarctic Peninsula). *Tectonophysics*, **259**, 275–301.
- GALLAND, O. & SCHEIBERT, J. 2013. Analytical model of surface uplift above axisymmetric flat-lying magma intrusions: implications for sill emplacement and geodesy. *Journal of Volcanology and Geothermal Research*, **253**, 114–130.
- GARCIA, M.A., LÓPEZ, O., SOSPEDRA, J., ESPINO, M., GRÀCIA, V., MORRISON, G., *et al.* 1994. Mesoscale variability in the Bransfield Strait region (Antarctica) during austral summer. *Annales Geophysicae*, **12**, 856–867.
- GEYER, A., PEDRAZZI, D., ALMENDROS, J., BERROSO, M., LÓPEZ-MARTÍNEZ, J., MAESTRO, A., *et al.* 2021. Deception Island. In SMELLIE, J.L., PANTER, K.S. & GEYER, A., eds, *Volcanism in Antarctica: 200 million years of subduction, rifting and continental break-up*. Geological Society, London, Memoirs, **55**, 667–693.
- GONZÁLEZ-CASADO, J.M., GINER-ROBLES, J. & LÓPEZ-MARTÍNEZ, J. 2000. Bransfield Basin, Antarctic Peninsula: not a normal backarc basin. *Geology*, **28**, 1043–1046.
- GONZÁLEZ-CASADO, J.M., LÓPEZ-MARTÍNEZ, J., GINER, J.L., DURÁN, J.J. & GUMIEL, P. 1999. Análisis de la microfracturación en la Isla Decepción, Antártida Occidental. *Geogaceta*, **26**, 31–34.
- GONZÁLEZ-FERRÁN, O. 1985. Volcanic and tectonic evolution of the northern Antarctic Peninsula - Late Cenozoic to Recent. *Tectonophysics*, **114**, 389–409.
- GONZÁLEZ-FERRÁN, O. & KATSUI, Y. 1970. Estudio integral del volcanismo cenozoico superior de las islas Shetland del Sur, Antártica. *Instituto Antártico Chileno, Serie Científica*, **1**, 123–174.
- GRÀCIA, E., CANALS, M., FARRÁN, M., SORRIBAS, J. & PALLÀS, R. 1997. Central and eastern Bransfield basins (Antarctica) from high-resolution swath-bathymetry data. *Antarctic Science*, **4**, 469–476.
- GRÀCIA, E., CANALS, M., FARRÁN, M., PRIETO, M.J., SORRIBAS, J. & GEBRA TEAM. 1996. Morphostructure and evolution of the central and eastern Bransfield Basins (NW Antarctic Peninsula). *Marine Geophysical Researches*, **18**, 429–448.
- GRAD, M., GUTERCH, A. & SRODA, P. 1992. Upper crustal structure of Deception Island area, Bransfield Strait, West Antarctica. *Antarctic Science*, **4**, 469–476.
- GUDMUNDSSON, A. & PHILIPP, S.L. 2006. How local stresses prevent volcanic eruptions. *Journal of Volcanology and Geothermal Research*, **158**, 257–268.
- HAASE, K.M., BEIER, C., FRETZDORFF, S., SMELLIE, J.L. & GARBE-SCHÖNBERG, D. 2012. Magmatic evolution of the South Shetland Islands, Antarctica, and implications for continental crust formation. *Contributions to Mineralogy and Petrology*, **163**, 1103–1119.
- HAWKES, D.D. 1961. The geology of the South Shetland Islands. II. The geology and petrology of Deception Island. *Falkland Islands Dependencies Scientific Reports*, **27**, 51 pp.
- HETÉNYI, G., TAISNE, B., GAREL, F., MÉDARD, É., BOSSHARD, S. & MATTSSON, H. 2012. Scales of columnar jointing in igneous rocks: field measurements and controlling factors. *Bulletin of Volcanology*, **74**, 457–482.
- HOLOHAN, E.P., TROLL, V.R., WALTER, T.R., MÜNN, S., McDONNELL, S. & SHIPTON, Z.K. 2005. Elliptical calderas in active tectonic settings: an experimental approach. *Journal of Volcanology and Geothermal Research*, **144**, 119–136.
- HOPFENBLATT, J., GEYER, A., AULINAS, M., ÁLVAREZ-VALERO, A.M., GISBERT, G., KERESZTURI, G., *et al.* 2021. Formation of Stanley Patch volcanic cone: new insights into the evolution of Deception Island caldera (Antarctica). *Journal of Volcanology and Geothermal Research*, **415**, 10.1016/j.jvolgeores.2021.107249.
- IBÁÑEZ, J.M., CARMONA, E., ALMENDROS, J., SACCOROTTI, G., DEL PEZZO, E., ABRIL, M. & ORTIZ, R. 2003. The 1998–1999 seismic series at Deception Island volcano, Antarctica. *Journal of Volcanology and Geothermal Research*, **128**, 65–88.

- JACKSON, M.D. & POLLARD, D.D. 1990. Flexure and faulting of sedimentary host rocks during growth of igneous domes, Henry Mountains, Utah. *Journal of Structural Geology*, **12**, 185–206.
- JAEGER, J.C. 1960. Shear failure of anisotropic rock. *Geology Magazine*, **97**, 6–72.
- JIMÉNEZ-MORALES, V. 2021. *Estudio sismológico de la actividad y estructura del Volcán Isla Decepción (Antártida), mediante el análisis de datos continuos registrados en una estación sísmica permanente (2008–2015)*. Doctoral thesis. Universidad de Granada, 259 pp.
- KATTENHORN, S.A. & SCHAEFER, C.J. 2008. Thermal-mechanical modeling of cooling history and fracture development in inflationary basalt lava flows. *Journal of Volcanology and Geothermal Research*, **170**, 181–197.
- KELLER, R.A., FISK, M.R., WHITE, W.M. & BIRKENMAJER, K. 1992. Isotopic and trace element constraints on mixing and melting models of marginal basin volcanism, Bransfield Strait, Antarctica. *Earth and Planetary Science Letters*, **111**, 287–303.
- KIYOSUGI, K., CONNOR, C., WETMORE, P., FERWERDA, B.P., GERMA, A., CONNOR, L.J. & HINTZ, M. 2012. Relationship between dike and volcanic conduit distribution in a highly eroded monogenetic volcanic field: San Rafael Utah, USA. *Geology*, **40**, 695–698.
- KOMURO, H. 1987. Experiments on cauldron formation: a polygonal cauldron and ring fractures. *Journal of Volcanology and Geothermal Research*, **31**, 139–149.
- KUCKARTZ, U., RÄDIKER, A., EBERT, T. & SCHEHL, J. 2013. *Statistik. Eine verständliche Einführung*. VS Verlag für Sozialwissenschaften Wiesbaden, XII, 301 pp.
- KUSAKABE, M., NAGAO, K., OHBA, T., SEO, J.H., PARK, S-H, LEE, J.I. & PARK, B-K. 2009. Noble gas and stable isotope geochemistry of thermal fluids from Deception Island, Antarctica. *Antarctic Science*, **21**, 255–267.
- LAWVER, L.A., KELLER, R.A., FISK, M.R. & STRELIN, J. 1995. Bransfield Strait, Antarctic Peninsula: active extension behind a dead arc. In TAYLOR, B., ed., *Back-arc basins: tectonics and magmatism*. New York: Plenum, 315–342.
- LAWVER, L.A., SLOAN, B.J., BARKER, D.H.N., GHIDELLA, M., VON HERZEN, R.P., KELLER, R.A., et al. 1996. Distributed, active extension in Bransfield Basin, Antarctic Peninsula: evidence from multibeam bathymetry. *GSA Today*, **6**, 1–6.
- LISTER, J.R. & KERR, R.C. 1991. Fluid-mechanical models of crack propagation and their application to magma transport in dykes. *Journal Geophysical Research*, **96**, 10049–10077.
- LOPES, F.C., CASELLI, A.T., MACHADO, A. & BARATA, M.T. 2015. The development of the Deception Island volcano caldera under control of the Bransfield Basin sinistral strike-slip tectonic regime (NW Antarctica). In PLATZ, T., MASSIRONI, M., BYRNE, P.K. & HIESINGER, H., eds, *Volcanism and tectonism across the inner solar system*. Geological Society, London, Special Publications, **401**, 173–184.
- LÓPEZ-MARTÍNEZ, J. & SERRANO, E. 2002. Geomorphology. In LÓPEZ-MARTÍNEZ, J., SMELLIE, J.L., THOMSON, J.W. & THOMSON, M.R.A., eds, *Geology and geomorphology of Deception Island*. BAS GEOMAP Series, Sheets 6-A and 6-B, 1:25 000, with supplementary text. Cambridge: British Antarctic Survey, 31–39.
- LÓPEZ-MARTÍNEZ, J., SERRANO, E., REY, J. & SMELLIE, J.L. 2000. Geomorphological map of Deception Island. Sheet 6-B. 1:25,000. In LÓPEZ-MARTÍNEZ, J., SMELLIE, J.L., THOMSON, J.W., & THOMSON, M.R.A., eds, 2002. *Geology and geomorphology of Deception Island*. BAS GEOMAP Series, Sheets 6-A and 6-B, with supplementary text. Cambridge: British Antarctic Survey, n.p.
- LÓPEZ-MARTÍNEZ, J., SMELLIE, J.L., THOMSON, J.W. & THOMSON, M.R.A., eds. 2002. *Geology and geomorphology of Deception Island*. BAS GEOMAP Series, Sheets 6-A and 6-B. Cambridge: British Antarctic Survey, 77 pp. and 3 maps.
- LÓPEZ-MARTÍNEZ, J., RAMOS, M., CRIADO, C., SERRANO, E. & NICOLÁS, P. 1996. Anomalías geotérmicas y permafrost en la Isla Decepción. In *Actas V Simposio Español de Estudios Antárticos*. Madrid: Comisión Interministerial de Ciencia y Tecnología, 223–234.
- MAESTRO, A., LÓPEZ-MARTÍNEZ, J., GALINDO-ZALDÍVAR, J., BOHOYO, F. & MINK, S. 2014. Evolution of the stress field in the southern Scotia Arc from the late Mesozoic to the present-day. *Global and Planetary Change*, **123**, 269–297.
- MAESTRO, A., SOMOZA, L., REY, J., MARTÍNEZ-FRÍAS, J. & LÓPEZ-MARTÍNEZ, J. 2007. Active tectonics, fault patterns and stress field of Deception Island: a response to oblique convergence between the Pacific and Antarctic plates. *Journal of South American Earth Sciences*, **23**, 256–268.
- MARTÍ, J., BARALDO, A. & REY, J. 1990. Origen y estructura de la Isla Decepción (Islas Shetland del Sur). In *Actas III Simposio Nacional de Estudios Antárticos*. Madrid: Comisión Interministerial de Ciencia y Tecnología, 187–194.
- MARTÍ, J., GEYER, A. & AGUIRRE-DÍAZ, G. 2013. Origin and evolution of the Deception Island caldera (South Shetland Islands, Antarctica) *Bulletin of Volcanology*, **75**, 1–18.
- MARTÍ, J., VILA, J. & REY, J. 1996. Deception Island (Bransfield Strait, Antarctica): an example of a volcanic caldera developed by extensional tectonics. In MCGUIRE, W.J., JONES, A.P. & NEUBERG, J., eds, *Volcano instability on the Earth and other planets*. Geological Society Special Publication, **110**, 253–265.
- MAZZARINI, F., LE CORVEC, N., ISOLA, I. & FAVALLI, M. 2016. Volcanic field elongation, vent distribution, and tectonic evolution of a continental rift: the Main Ethiopian Rift example. *Geosphere*, **12**, 706–720.
- MCCARRON, J.J. & LARTER, R.D. 1998. Late Cretaceous to early Tertiary subduction history of the Antarctic Peninsula. *Journal of the Geological Society*, **155**, 255–268.
- MERIAUX, C., LISTER, J.R., LYAKHOVSKY, V. & AGNON, A. 1999. Dyke propagation with distributed damage of the host rock. *Earth Planetary Science Letters*, **165**, 177–185.
- MORENO-VACAS, A. & ALMENDROS, J. 2021. On the origin of recent seismic unrest episodes at Deception Island volcano, Antarctica. *Journal of Volcanology and Geothermal Research*, **419**, 107376.
- MUNIZ, M.C., ANJOS, R.M., CARDOSO, R.P., ROSA, L.H., VIEIRA, R., MAROTTA, H., et al. 2018. Post-caldera evolution of Deception Island (Bransfield Strait, Antarctica) over Holocene timescales. *Palaeogeography, Palaeoclimatology, Palaeoecology*, **501**, 58–69.
- MUÑOZ-MARTÍN, A., CATALÁN, M., MARTÍN-DÁVILA, J. & CARBÓ, A. 2005. Upper crustal structure of Deception Island area (Bransfield Strait, Antarctica) from gravity and magnetic modelling. *Antarctic Science*, **17**, 213–224.
- NAVARRO, F.J., VÉLEZ, E.J., CAMACHO, A.G. & VIEIRA, R. 2002. A gravity survey of Deception Island (South Shetland Islands, Antarctica). *Royal Society New Zealand Bulletin*, **35**, 515–524.
- OLIVA-URCÍA, B., GIL-PEÑA, I., MAESTRO, A., LÓPEZ-MARTÍNEZ, J., GALINDO-ZALDÍVAR, J., SOTO, R., et al. 2015. Paleomagnetism from Deception Island (South Shetlands archipelago, Antarctica), new insights into the interpretation of the volcanic evolution using a geomagnetic model. *International Journal of Earth Sciences*, **105**, 1353–1370.
- ORHEIM, O. 1972. *A 200-year record of glacier mass balance at Deception Island, southwest Atlantic Ocean, and its bearing on models of global climate change*. Institute of Polar Studies Report, **42**. Columbus, OH: Research Foundation and the Institute of Polar Studies, Ohio State University, 118 pp.
- ORTIZ, R., GARCÍA, A., APARICIO, A., BLANCO, I., FELPETO, A., DEL-REY, R., et al. 1997. Monitoring of the volcanic activity of Deception Island, South Shetland Islands, Antarctica (1986–1995). In RICCI, C.A., ed., *The Antarctic region: geological evolution and processes*. Siena: Terra Antarctica Publication, 1071–1076.
- PAREDES, C., DE LA VEGA, R., PÉREZ-LÓPEZ, R., GINER-ROBLES, J.L. & MARTÍNEZ-DÍAZ, J.J. 2007. Descomposición fractal en subdominios morfotectónicos del mapa de lineamientos morfológicos en la isla Decepción (Shetland del Sur, Antártida). *Boletín Geológico y Minero*, **118**, 775–787.
- PAREDES, C., PÉREZ-LOPEZ, R., GINER-ROBLES, J.L., DE LA VEGA, R., GARCÍA-GARCÍA, A. & GUMIEL, P. 2006. Distribución espacial y zonificación tectónica de los morfolineamientos en la Isla Decepción (Shetland del Sur, Antártida). *Geogaceta*, **39**, 75–78.
- PEDRAZZI, D., NÉMETH, K., GEYER, A., ÁLVAREZ-VALERO, A.M., AGUIRRE-DÍAZ, G. & BARTOLINI, S. 2018. Historic hydrovolcanism at Deception Island (Antarctica): implications for eruption hazards. *Bulletin of Volcanology*, **80**, 11.
- PEDRAZZI, D., KERESZTURI, G., LOBO, A., GEYER, A. & CALLE, J. 2020. Geomorphology of the post-caldera monogenetic volcanoes at Deception Island, Antarctica - implications for landform recognition and volcanic hazard assessment. *Journal of Volcanology and Geothermal Research*, **402**, 106986.
- PEDRERA, A., RUIZ-CONSTÁN, A., HEREDIA, N., GALINDO-ZALDÍVAR, J., BOHOYO, F., MARÍN-LECHADO, C., et al. 2012. The fracture system and

- the melt emplacement beneath the Deception Island active volcano, South Shetland Islands, Antarctica. *Antarctic Science*, **24**, 173–182.
- PÉREZ-LÓPEZ, R., FERNÁNDEZ-IBÁÑEZ, F., MARTÍNEZ-DÍAZ, J.J., PAREDES, C., GINER, J.L. & CASELLI, A. 2004. Criterios geomorfológicos sobre actividad tectónica reciente a lo largo de la Costa Recta, Isla Decepción (Antártida Occidental). *Geo-Temas*, **6**, 179–182.
- PÉREZ-LÓPEZ, R., GINER-ROBLES, J.L., BÉJAR, M., RODRÍGUEZ-PASCUA, M.A., MARTÍNEZ-DÍAZ, J.J., PAREDES, C. & GONZÁLEZ-CASADO, J.M. 2008. Determinación del campo de esfuerzo/deformación activo en una isla volcánica a partir de técnicas fractales y estructurales (Isla Decepción, Antártida Occidental). *Geo-Temas*, **10**, 397–400.
- PÉREZ-LÓPEZ, R., GINER-ROBLES, J.L., MARTÍNEZ-DÍAZ, J.J., RODRÍGUEZ-PASCUA, M.A., BEJAR, M., PAREDES, C. & GONZÁLEZ-CASADO, J.M. 2007. Active tectonics on Deception Island (West-Antarctica): a new approach by using the fractal anisotropy of lineaments, fault slip measurements and the caldera collapse shape. In COOPER, A.K., BARRETT, P., STAGG, H., STOREY, B., STUMP, E. & WISE, W., eds, *Antarctica: a keystone in a changing world. Online proceedings of the 10th ISAES*, USGS Open-File Report 2007-1047, Short Research Paper 086. Washington, DC: National Academies Press, 4 pp.
- PRIETO, M.J., CANALS, M., ERCILLA, G. & DE BATIST, M. 1998. Structure and geodynamic evolution of the central Bransfield Basin (NW Antarctica) from seismic reflection data. *Marine Geology*, **149**, 17–38.
- PUEYO, O., GIL IMAZ, A., GIL-PEÑA, I., MAESTRO, A., GALINDO-ZALDÍVAR, J., LÓPEZ-MARTÍNEZ, J., et al. 2014. Application of AMS for reconstruction of the geological evolution of recent volcanic systems: case of Deception Island (South Shetland Islands, Antarctica). *Tectonophysics*, **626**, 69–85.
- REY, J., DE ANDRÉS, J.R. & FERNÁNDEZ-LÓPEZ, J.M. 1990. Tectónica reciente en los depósitos submarinos de la bahía de Decepción. In *Actas III Simposio Nacional de Estudios Antárticos*, Madrid: Comisión Interministerial de Ciencia y Tecnología, 258–270.
- REY, J., SOMOZA, L. & HERNÁNDEZ-MOLINA, F.J. 1992. Formas de los sedimentos submarinos superficiales en el Puerto Foster, Isla Decepción, Islas Shetland del Sur. In LÓPEZ-MARTÍNEZ, J., ed., *Geología de la Antártida Occidental, III Congreso Geológico de España y VIII Congreso Latinoamericano de Geología*. Salamanca: Simposios T3, 163–172.
- REY, J., SOMOZA, L. & MARTÍNEZ-FRÍAS, J. 1995. Tectonic, volcanic and hydrothermal event sequence on Deception Island (Antarctica). *Geo-Marine Letters*, **15**, 1–8.
- REY, J., SOMOZA, L. & MARTÍNEZ-FRÍAS, J. 1996. Evidencias tectónicas, volcánicas e hidrotermales en Isla Decepción, relacionadas con el marco geodinámico de la cuenca de Bransfield (Antártida). In CACHO, J. & SERRAT, D., eds, *Actas del V Simposio de Estudios Antárticos*. Madrid: Comisión Interministerial de Ciencia y Tecnología, 209–222.
- REY, J., MAESTRO, A., SOMOZA, L. & SMELLIE, J.L. 2002. Submarine morphology and seismic stratigraphy of Port Foster. In LÓPEZ-MARTÍNEZ, J., SMELLIE, J.L., THOMSON, J.W. & THOMSON, M.R.A., eds, *Geology and geomorphology of Deception Island. BAS GEOMAP Series, Sheets 6-A and 6-B*, **1**: 25 000. Cambridge: British Antarctic Survey, 40–46.
- REY, J., SOMOZA, L., MARTÍNEZ-FRÍAS, J., BENITO, R. & MARTÍN-ALFAGEME, S. 1997. Deception Island (Antarctica): a new target for exploration of Fe-Mn mineralization? In NICHOLSON, K., HEIN, J.R., BIRN, B. & DASGUPTA, S., eds, *Manganese mineralization: geochemistry and mineralogy of terrestrial and marine deposits*. London: Geological Society Special Publication, **119**, 239–251.
- RIVALTA, E., TAISNE, B., BUNGER, B.P. & KATZ, R.F. 2015. A review of mechanical models of dike propagation: schools of thought, results and future directions. *Tectonophysics*, **638**, 1–42.
- ROCHE, O., DRUITT, T.H. & MERLE, O. 2000. Experimental study of caldera formation. *Journal of Geophysical Research - Solid Earth*, **105**, 395–416.
- RUBIN, A.M. 1995. Propagation of magma-filled cracks. *Annual Review of Earth and Planetary Sciences*, **23**, 287–336.
- RUBIN, A.M. & POLLARD, D.D. 1988. Dike-induced faulting in rift zones of Iceland and Afar. *Geology*, **16**, 413–417.
- SCANVIC, J.Y. 1989. *Teledetección Aplicada. Cartografía, geología estructural, exploración minera, medio ambiente, etc.* Madrid: Ediciones Paraninfo, S.A., 208 pp.
- SCHOFIELD, N., BROWN, D.J., MAGEE, C. & STEVENSON, C.T. 2012. Sill morphology and comparison of brittle and non-brittle emplacement mechanisms. *Journal of the Geological Society*, **169**, 127–141.
- SENGER, K., BUCKLEY, S.J., CHEVALLIER, L., FAGERENG, A., GALLAND, O., KURZ, T.H., et al. 2015. Fracturing of doleritic intrusions and associated contact zones: implications for fluid flow in volcanic basins. *Journal of African Earth Sciences*, **102**, 70–85.
- SHESKIN, D.J. 2000. *Handbook of parametric and nonparametric statistical procedures*, 2nd edition. New York: Chapman and Hall/CRC Press, 972 pp.
- SILVERMAN, B.W. 1986. *Density estimation for statistics and data analysis. Monographs on Statistics and Applied Probability*. New York: Chapman & Hall/CRC Press, 176 pp.
- SMELLIE, J.L. 1988. Recent observations on the volcanic history of Deception Island, South Shetland Islands. *British Antarctic Survey Bulletin*, **81**, 83–85.
- SMELLIE, J.L. 2001. Lithostratigraphy and volcanic evolution of Deception Island, South Shetland Islands. *Antarctic Science*, **13**, 188–209.
- SMELLIE, J.L. 2002. Geology. In LÓPEZ-MARTÍNEZ, J., SMELLIE, J.L., THOMSON, J.W. & THOMSON, M.R.A., eds, *Geology and geomorphology of Deception Island. BAS GEOMAP Series, Sheets 6-A and 6-B*. Cambridge: British Antarctic Survey, 11–30.
- SMELLIE, J.L. & LÓPEZ-MARTÍNEZ, J. 2000. Geological map of Deception Island. In LÓPEZ-MARTÍNEZ, J., SMELLIE, J.L., THOMSON, J.W. & THOMSON, M.R.A., eds, *Geology and geomorphology of Deception Island. BAS GEOMAP Series, Sheets 6-A and 6-B with supplementary text*. Cambridge: British Antarctic Survey, n.p.
- SMELLIE, J.L. & LÓPEZ-MARTÍNEZ, J. 2002. Introduction. In LÓPEZ-MARTÍNEZ, J., SMELLIE, J.L., THOMSON, J.W. & THOMSON, M.R.A., eds, *Geology and geomorphology of Deception Island. BAS GEOMAP Series, Sheets 6-A and 6-B*. Cambridge: British Antarctic Survey, 1–6.
- SMELLIE, J.L., PANTER, K.S. & GEYER, A., eds. 2021. *Volcanism in Antarctica: 200 million years of subduction, rifting and continental break-up*. London: Geological Society, London, Memoirs, **55**, 10.1144/M55.
- SOMOZA, L., MARTÍNEZ-FRÍAS, J., SMELLIE, J.L., REY, J. & MAESTRO, A. 2004. Evidence for hydrothermal venting and sediment volcanism discharged after recent short-lived volcanic eruptions at Deception Island, Bransfield Strait, Antarctica. *Marine Geology*, **34**, 119–140.
- TOKARCZYK, R. 1987. Classification of water masses in the Bransfield Strait and southern part of the Drake Passage using a method of statistical multidimensional analysis. *Polish Polar Research*, **8**, 333–336.
- TORRECILLAS, C., BERROCOZO, M., FELPETO, A., TORRECILLAS, M.D. & GARCÍA, A. 2013. Reconstructing palaeo-volcanic geometries using a geodynamic regression model (GRM): application to Deception Island volcano (South Shetland Islands, Antarctica). *Geomorphology*, **182**, 79–88.
- TROLL, V.R., WALTER, T.R. & SCHMINCKE, H.U. 2002. Cyclic caldera collapse: piston or piecemeal subsidence? Field and experimental evidence. *Geology*, **30**, 135–138.
- VALENCIO, A., MENDÍA, E. & VILAS, J. 1979. Palaeomagnetism and K-Ar age of Mesozoic and Cenozoic igneous rocks from Antarctica. *Earth and Planetary Science Letters*, **45**, 61–68.
- VILA, A., MARTÍ, J., ORTIZ, R., GARCÍA, A. & CORREIG, A. 1992. Volcanic tremors at Deception Island. *Journal of Volcanology and Geothermal Research*, **53**, 89–102.
- VILLEGAS, M.T., CASELLI, A. & GARCÍA, A. 1997. *Nuevas aportaciones al estudio de las variaciones estacionales de los gases volcánicos de la Isla Decepción (Islas Shetland del Sur)*. Boletín Real Sociedad Española de Historia Natural (Sección Geología), **93**, 145–153.
- WALTER, T.R. & TROLL, V.R. 2001. Formation of caldera periphery faults: an experimental study. *Bulletin of Volcanology*, **63**, 191–203.
- WISE, D.U. & McCRORY, T.A. 1982. A new method of fracture analysis: azimuth versus distance plots. *Geological Society of America Bulletin*, **93**, 889–897.
- WOODCOCK, N.H. & FISCHER, M. 1986. Strike-slip duplexes. *Journal of Structural Geology*, **8**, 725–735.
- ZOBIN, V.M. 2014. Volcano seismology: an introduction. In MEYERS R.A., ed., *Encyclopedia of complexity and systems science*. Berlin: Springer, 10.1007/978-3-642-27737-5_607-2.